

# Band Gap Narrowing in Silane-grafted ZnO Nanocrystals. A Comprehensive Study by Wide-angle X-ray Total Scattering Methods

Federica Bertolotti,<sup>a</sup> Aurel Tăbăcaru,<sup>\*b</sup> Viorica Muşat,<sup>b</sup> Nicolae Țigău,<sup>b</sup> Antonio Cervellino,<sup>c</sup> Norberto Masciocchi,<sup>\*a</sup> and Antonietta Guagliardi<sup>\*d</sup>

<sup>a</sup>*Dipartimento di Scienza e Alta Tecnologia and To.Sca.Lab, Università dell'Insubria, via Valleggio 11, I-22100 Como, Italy.*

<sup>b</sup>*Center of Nanostructures and Functional Materials – CNMF, Department of Materials Science and Engineering, Faculty of Engineering, Dunărea de Jos University of Galati, 111 Domneasca Street, 800201, Galași, Romania.*

<sup>c</sup>*SLS, Laboratory for Synchrotron Radiation - Condensed Matter, Paul Scherrer Institut, CH-5232 Villigen, Switzerland.*

<sup>d</sup>*Istituto di Cristallografia and To.Sca.Lab, Consiglio Nazionale delle Ricerche, via Valleggio 11, I-22100 Como, Italy.*

**KEYWORDS.** Zinc oxide, nanocrystals, organosilane surface modification, X-ray wide angle scattering, Debye scattering equation, planar defects

**ABSTRACT:** Zinc oxide (ZnO) is a largely investigated semiconducting nanomaterial for photocatalytic applications and is an excellent active layer candidate in photovoltaics. Among native defects, having a primary role in ZnO optoelectronic properties, the influence of nearly ubiquitous planar faults of wurtzite sequences in ultrasmall ( $\leq 5$  nm) nanocrystals (NCs) remains poorly understood. Here, we present a thorough study of ZnO NCs prepared under morphological control of covalently grafted vinyltrimethoxysilane (VTMS) and exhibiting either narrowing or widening of the band gap upon NCs downsizing, depending on NCs growth rate. By using synchrotron X-ray total scattering data, atomistic models and the Debye Scattering Equation (DSE) method, complemented by spectroscopic (FTIR and UV-vis) investigations, we provide a comprehensive quantitative picture in which effects from planar defects are disentangled from those due to NCs size, morphology and lattice strain (here controlled by preferential binding of VTMS on the ZnO basal faces). When faults occur in high concentration (linear density up to  $1.6 \times 10^6 \text{ cm}^{-1}$ ), NCs exhibit optical band gap narrowing (3.27 eV vs 3.37 eV in bulk ZnO), whereas gap widening (3.52 eV) is observed at lower density ( $0.8 \times 10^6 \text{ cm}^{-1}$ ), where quantum-size confinement effects prevail. Supported by photoluminescence and photodegradation experiments, surface defect passivation by VTMS, affecting visible emissions and photocatalytic properties of ZnO, is also discussed in relation to silane coating and fault-driven bandgap. This work sheds light on the complex interplay among planar defects, quantum size effect and surface modifications in ultrasmall ZnO NCs and on the importance of advanced X-ray total scattering methods towards atomically precise control of defects in nanostructures.

## 1. INTRODUCTION

Zinc oxide (ZnO) nanoparticles exhibit uncommon optoelectronic properties attracting, over the last decades, a deal of attention likely equated (for semiconducting oxide nanomaterials) only by titanium dioxide nanoparticles. Nanoscaling and nanostructuring have intriguingly expanded the well-known intrinsic properties of bulk ZnO (wide direct band gap, 3.37 eV, and high exciton energy, 60 meV) that make it an excellent candidate material for UV applications,<sup>1–3</sup> with gained interest in a wider range of fields (photovoltaics, catalysis, chemical and bio-sensing, light emitting devices, lasing, thermoelectrics, surface plasmonic resonance).<sup>4–16</sup> The material versatility is further favoured by cost-effective large-scale ZnO production and low tempera-

ture processability, jointly to a variety of preparation methods for the control over NPs size and morphology, surface modification, stability and toxicity issues.<sup>17–25</sup>

Among these, grafting by organosilanes has been emerging as an extremely attractive strategy.<sup>15,26–32</sup> Besides the advantage of rapid formation of stable covalent bonds between the NCs surface and the alkoxy silane anchoring groups (supported by IR and NMR investigations),<sup>26,33,34</sup> a library of flexible residuals acting as end-group can be used for further tuning the ZnO NCs physico-chemical properties. Relevant cases of study and application include: aminopropyltriethoxysilane (APTS-modified ZnO NCs were implemented as the active layer of new hybrid light emitting devices with optimized performances)<sup>31</sup> and 3-aminopropyltrimethoxysilane (APTMS-grafted ZnO NCs were successfully used as the electron transport layer in inverted

organic solar cells, with very promising results for roll-to-roll printing photovoltaics);<sup>32</sup> vinyltrimethoxysilane (VTMS)<sup>29</sup> and 3-(trimethoxysilyl)propylmetacrylate (MPS),<sup>28</sup> with enhanced photoluminescence; the hydrophobic hexadecyltrimethoxysilane (HDS) and hydrophilic APTS bilayers with high stability in aqueous media and tunable fluorescence for tissue imaging;<sup>15</sup> the 3-(glycidyloxypropyl)trimethoxysilane (GPTMS) showing increased antibacterial activity and cytotoxicity in human cancer cells at very small NPs size.<sup>30</sup>

One intriguing property of VTMS-grafted ZnO NCs,<sup>29</sup> observed also with MPS grafting,<sup>28</sup> is the unusual decrease of the energy optical band gap upon NCs downsizing ( $\leq 5$  nm), in contrast to what expected for quantum confinement effects. In the present work, we focus on this mesmerising property of VTMS-grafted ZnO NCs, with the aim of shedding light on its origin and further investigating the possible influence on surface defects passivation. With reference to the characteristic emissions of ZnO, they are typically observed in the near UV (attributed to radiative recombination of electron-hole from conduction-valence bands or excitons bound to shallow donors),<sup>35</sup> and in the green visible region (due to recombination from localized states that, though highly debated, are mainly ascribed to vacancies and to the deep trap states generated therefrom).<sup>36</sup> Native defects are known to have a primary role in ZnO optoelectronic properties, particularly those related to Zn and O vacancies and interstitial atoms.<sup>37–41</sup>

As found in many other II-VI semiconductors, stacking faults (SFs) are one of the most common structural defects in ZnO.<sup>42</sup> Nonetheless, their clear-cut effect on the bandgap energy of NCs is poorly understood, owing to the interplay with effects controlled by finite-size (quantum confinement),<sup>43</sup> morphology and large specific surface area (where vacancy defects are mostly located).

The hexagonal wurtzite-like structure (built upon hcp Zn and O sub-lattices) is highly stabilized by the formation of short distances between ions of opposite charge in the eclipsed configuration of  $\text{ZnO}_4$ -tetrahedra,<sup>42</sup> making the wurtzite packing the (solely known) stable ZnO polymorph at ambient conditions. Nevertheless, mistakes due to the formation of layers with the staggered (zincblende type) cubic configuration are common, particularly in low-temperature preparation methods and in the absence of robust post-synthetic thermal treatments. Compared to other II-VI semiconductors, the SF energy is quite high in ZnO ( $100 \text{ mJ m}^{-2}$  vs  $14 \text{ mJ m}^{-2}$  in CdSe).<sup>44</sup> The density of planar defects is typically reported within 1–2% (that is, ca.  $0.4$  to  $0.8 \times 10^6 \text{ cm}^{-1}$ , in bulk or annealed ZnO NCs few tens of nm large), making them easily detectable, for example, by X-ray analysis.<sup>45–47</sup> SF concentration as high as  $10^6 \text{ cm}^{-1}$  in micrometre-long nanowires were also measured via helium ion microscopy (HIM) with sub-nanometre resolution.<sup>48</sup>

In bulk ZnO, computational studies suggest that a high density of planar defects ( $> 1.0 \times 10^6 \text{ cm}^{-1}$ ) may lower the conduction band level, therefore suggesting a feasible origin for the band-gap narrowing detected in VTMS-grafted ZnO NCs.<sup>49</sup> However, elucidating the precise influence of nearly ubiquitous planar defects on the optoelectronic properties of ultrasmall ZnO NCs remains a highly challenging task. Here, we performed an in-depth characterization of VTMS-grafted ZnO NCs prepared with increasing amount of silane

(Si/Zn molar ratio in the 0–15% range) and provide a quantitative and comprehensive determination of intermingled atomic-to-nanoscale features, such as size, morphology and density of planar defects. To this aim, we applied an advanced data-analysis procedure based on synchrotron Wide Angle X-ray Total Scattering (WAXTS) data in combination with the Debye Scattering Equation (DSE) method,<sup>50,51</sup> and an originally developed atomistic model of ZnO NCs where size, morphology, stacking faults and lattice strain were jointly considered within a unified description.

WAXTS analysis remains unique in exploring defectiveness at atomic resolution while simultaneously providing statistically robust measures of nanometre-scale distribution properties of the ensemble, offering a powerful multiscale approach (yet not fully exploited).<sup>50,52,53</sup> Notably, through synchrotron experiments, all sources of scattering (from the sample and environment) can be precisely controlled. On the modelling side, the DSE is a unique tool for calculating both Bragg and diffuse X-ray scattering (using the set of interatomic distances computed from the atomistic model, as detailed in the Experimental Section) in reciprocal space, enabling calculated and experimental patterns to be directly matched.

Presently, WAXTS and customized DSE-based analysis have been successfully developed for different classes of engineered nanomaterials, ranging from metals to metal oxides, bioceramics, lead halide perovskites and also II-VI quantum dots with a high density of planar defects.<sup>54–62</sup> Herein, we developed the approach for VTMS-grafted ZnO NCs; the influence of the crystal growth rate on the structural defects (beyond size, morphology and surface modification), was further investigated in samples isolated after either fast (3 hours) or slow (one week) maturation in the reaction solution. We present a comprehensive analysis of these two series. Results are discussed in relation to changes in the optical band gap energy and photoluminescence (by UV-vis reflectance and PL spectroscopy), and in photodegradation experiments.

## 2. EXPERIMENTAL SECTION

**Materials.** Zinc acetate dihydrate (purity  $> 98\%$ ), methanol, vinyltrimethoxysilane (purity =  $98\%$ ) and potassium hydroxide were purchased from Sigma Aldrich and used without further purification.

**Synthesis of ZnO NCs.** ZnO nanoparticles were synthesized according to a method reported in literature.<sup>34</sup> Briefly, in 10 mL of methanol heated to  $55^\circ\text{C}$ , different amounts of vinyltrimethoxysilane were added in order to reach the Si/Zn molar ratio of 0%, 2% (33 mg), 5% (82.50 mg), 10% (165 mg) and 15% (247.50 mg). After a further heating to  $60^\circ\text{C}$  for 10 min, 2.45 g of zinc acetate dihydrate was added in the reaction vessel. Ten minutes later, a basic solution of 1.25 g of potassium hydroxide separately dissolved in 5 mL of methanol, was added dropwise. The white suspensions so obtained were stirred for 3 hours under reflux. After this time, the suspensions were cooled down and centrifuged (9000 rpm,  $10^\circ\text{C}$ , 5 min), washed with three portions of methanol, and finally dried at  $100^\circ\text{C}$  in an oven for 3 hours. The corresponding supernatant solutions were allowed to stand at room temperature, and after one week, new white and dense suspensions were obtained upon almost complete evaporation of methanol. They were washed with several portions of methanol and distilled water with centrifugation, then they were collected and dried at  $100^\circ\text{C}$  in an oven for 3 hours. Samples isolated from the fast precipitation

are labelled as  $\text{Si}_x\text{@ZnO}_{\text{fast}}$ , those isolated from the slow precipitation as  $\text{Si}_x\text{@ZnO}_{\text{slow}}$ , where  $x$  is the Si/Zn molar ratio ( $x = 0, 2, 5, 10$  and 15%).

**Synchrotron Wide Angle X-ray Total Scattering experiments (WAXTS).** WAXTS measurements of  $\text{Si}_x\text{@ZnO}_{\text{fast}}$  and  $\text{Si}_x\text{@ZnO}_{\text{slow}}$  samples were collected at the X04SA-MS beamline<sup>63</sup> of the Swiss Light Source (Paul Scherrer Institute, Villigen, CH) on dry powders loaded in 0.5 mm-diameter certified quartz capillaries. The operational beam energy was set at 22 keV ( $\lambda = 0.564184 \text{ \AA}$ ) and precisely determined using a Si powder standard (NIST 640d,  $a_0 = 0.543123(8) \text{ nm}$  at  $22.5^\circ\text{C}$ ). WAXTS data were collected in the  $0.2\text{--}19 \text{ \AA}^{-1}$  Q-range using a single photon counting silicon microstrip detector (MYTHEN II),<sup>64</sup> on the samples, the empty glass capillary and the environment (air), the last two to be subsequently subtracted from the sample patterns. The transmitted beam intensities from the filled capillaries were also measured in order to estimate the samples absorption coefficients, while the computed X-ray attenuation factors from the nominal composition were used for the empty capillary. Angular dependent intensities corrections to the raw data were applied, using locally developed routines.<sup>53</sup> The inelastic Compton scattering signal was added as an additional model component during the data analysis. For the DSE-model refinements, the  $0.6\text{--}17 \text{ \AA}^{-1}$  Q-range was used.

**The Debye Scattering Equation (DSE)-based approach.** The DSE provides the average differential cross-section of a randomly oriented powder from the distribution of interatomic distances between atomic pairs, within the sample:<sup>51</sup>

$$I(Q) = \sum_{j=1}^N f_j(Q)^2 o_j^2 + 2 \sum_{j>i}^N f_j(Q) f_i(Q) T_j(Q) T_i(Q) o_j o_i \frac{\sin(Qd_{ij})}{(Qd_{ij})}$$

where  $Q=2\pi q$ ,  $q=2\sin\theta/\lambda$  is the magnitude of the scattering vector,  $\lambda$  is the radiation wavelength,  $f_i$  is the X-ray atomic form factor of the element at site  $i$ ,  $d_{ij}$  is the interatomic distance between atomic sites  $i$  and  $j$ ,  $N$  is the total number of atomic sites and  $T_i$  and  $o_i$  are the thermal atomic displacement parameter and the site occupancy factor associated to each atomic site, respectively.

The standard DSE-based analysis performed by the *DebUsSy Suite*<sup>65</sup> is based on a bottom up, two-step approach. Populations of atomistic models of NCs of increasing sizes are generated in the first step, according to one ( $D$ , isotropic NCs) or two ( $D_{ab}$  and  $L_c$ , anisotropic NCs) growth directions. Equi-spaced Gaussian sampled interatomic distances and pseudo-multiplicities<sup>66</sup> are encoded in suitable databases, speeding up the DSE calculation. Structural ( $T$ ,  $o$ , strain parameters) and microstructural parameters (average sizes and their standard deviations according to a mono- or bivariate lognormal law) are refined against the experimental data in the second step, through an iterative procedure based on the Simplex method and standard  $\chi^2$  minimization.<sup>67</sup>

**ZnO NCs stacking faults modeling.** The close-packed hexagonal (*hcp*) structure of ZnO can be described by the stacking of double layers of (001) planes along the [001] direction. According to Pandey's notation,<sup>68</sup> the letter  $h$  indicates a hexagonal sequence and  $k$  a cubic one (an *hcp* stacking of planes becomes: ...*hhhh*... and a *fcc*: ...*kkkk*...). A mistake introduced in the regular stacking sequence will result in a basal-plane stacking fault, within the ZnO crystal structure. Growth faults occur with a single interruption of the regular stacking sequence (Figure S2, ...*AaBbAaBbCcBbCc*... or ...*hhkh*...); when two violations of the stacking rule appear, the mistakes are termed deformation or intrinsic stacking faults (Figure 1d: ...*AaBbAaBbCcAaCcAaBb*... or ...*hhkhkh*...).

The presence of such defects necessarily breaks the long-range periodicity of the NCs and demands the implementation of a "non-periodic" approach in order to model the WAXTS data. The presence of SF was taken into account in the atomistic model construction of ZnO NCs by assuming that any location of one or more faults in the atomic layer sequence has the same probability to occur. However, the percentage of defects in a material is typically un-

known and implies, on the modeling side, a description with adjustable fault density. According to the *DebUsSy Suite*<sup>65</sup> strategy, we developed a method with affordable CPU-time to deal with low SF density NCs, such as ZnO (expected values are in the 1-6% range). A detailed description of this approach, also applied to metallic faulted Pt NCs, can be found in ref. <sup>57</sup>; adaptations to the ZnO case are detailed in the Supporting Information file.

Accordingly, we built bivariate population of atomistic models of ZnO by convoluting the lattice nodes enclosed within a hexagonal surface of each basal plane with the ZnO unit (Figure 1b). This layer-by-layer construction allows the automatic generation of both regular and faulted stacking sequences along the [001] growth direction. This model includes the generations of all the possible combination of hexagonal bases and clusters heights (along the stacking direction), being the step between two consecutive sizes the diameter of the circle of equivalent area in  $ab$  (first growth direction) and two atomic layers along  $c$  (second growth direction).

Multiple populations of hexagonal shaped NCs were built (and encoded in suitable databases of Gaussian sampled interatomic distances), each of which refers to a selected deformation fault density,  $\alpha$ , up to the maximum value of 6.0%, in steps of 0.5%. Considering the suitable unit transformations, the stacking fault density  $\alpha$  is easily translated into the linear density  $2\alpha/c \cdot 10^6 \text{ cm}^{-1}$ , where  $c = 5.60 \text{ \AA}$  is the ZnO  $c$  axis length. Our original strategy to the problem relies on the assumption that a single defect per cluster forms within the bivariate population of NCs; the desired SF density is obtained by properly weighting the sampled interatomic distances of (equal-sized) *faulted* and *unfaulted* (i.e. periodic) clusters through a linear combination of their multiplicities, ending up with a single set of multiplicities for each NC size representing the "average" deformation (further details are given in the Supporting Information file).

**FTIR spectroscopy.** Fourier Transform Infrared spectra (FTIR) were recorded from 4000 to  $650 \text{ cm}^{-1}$  with a Perkin-Elmer Spectrum 100 instrument by total reflectance on a CdSe crystal (resolution of  $4 \text{ cm}^{-1}$ ). FTIR spectra of unmodified and VTMS-grafted ZnO nanoparticles prepared at Si/Zn molar ratio = 0 – 15% show the presence of a wide band centered at  $3400 \text{ cm}^{-1}$  that is assigned to the stretching modes of -OH groups exposed at the ZnO NCs surface and eventually to the presence of physisorbed water.<sup>26,31,69,70</sup> Two intense peaks at  $1570 \text{ cm}^{-1}$  and  $1417 \text{ cm}^{-1}$  are ascribed to the asymmetric and symmetric stretching modes, respectively, of -COO- moieties of residue acetate groups, not completely removed after the washing procedure.<sup>26,31</sup> FTIR spectra of the VTMS-capped ZnO samples show two additional bands at  $960 \text{ cm}^{-1}$  and  $880 \text{ cm}^{-1}$  (the latter becoming more intense while increasing Si/Zn amount) which are attributed to Si-O(H) from partially hydrolysed VTMS and symmetric Si-O-Si stretching vibrations, respectively.<sup>26,69,71</sup> The Zn-O-Si vibration is assigned near  $670 \text{ cm}^{-1}$  on the basis of the literature.<sup>72</sup>

The absence of the  $960 \text{ cm}^{-1}$  peak in the  $\text{Si}_2\text{@ZnO}_{\text{slow}}$  indicates the lack of (residual) silane grafted to ZnO NCs. The weak and broad band at  $880 \text{ cm}^{-1}$ , occurring in unmodified ZnO NCs is ascribed to  $\nu_2$  and  $\nu_4$  bending modes of  $\text{CO}_3^{2-}$ <sup>73,74</sup> due to  $\text{CO}_2$  adsorption on the zinc oxide surface, forming chelating or bridging carbonate species.<sup>75</sup>

**Optical measurements.** A Fluorolog iHR 320 Horiba Jobin Yvon spectrofluorimeter equipped with a PMT detector was used to acquire the steady-state PL spectra from solutions. Transmittance spectra were acquired at room temperature with a Perkin Elmer (Lambda 35) UV-vis-NIR spectrophotometer, operated in air, at normal incidence, in the  $190\text{--}1100 \text{ nm}$  spectral range. Specimens were prepared by dispersing the obtained nanoparticles by sonication in isopropanol and depositing as thin films on glass substrate by spin coating (2000 rpm, 20 s).

**Photocatalytic degradation of methylene blue.** The photocatalytic activity of VTMS-grafted ZnO NCs was evaluated through the bleaching of methylene blue (MB) aqueous solution (20 mL,

0.1%) in the presence of 0.05 g of powder, under UV illumination at 365 nm for 60 min. The bleaching of MB aqueous solution was quantitatively measured by UV-Vis absorption spectra performed with a Microplate reader with fluorescence spectrometer Infinite 200 PRO NanoQuant (Tecan, Switzerland), in the 400–800 nm range. The photocatalytic activity of the prepared ZnO photocatalysts was quantitatively evaluated by determining the photodegradation efficiency ( $\eta\%$ ) of MB:

$$\eta = \frac{A_0 - A}{A_0} \cdot 100$$

where  $A_0$  is the absorbance of the dye-containing solutions before UV illumination and  $A$  is the absorbance of the same solutions after UV illumination.

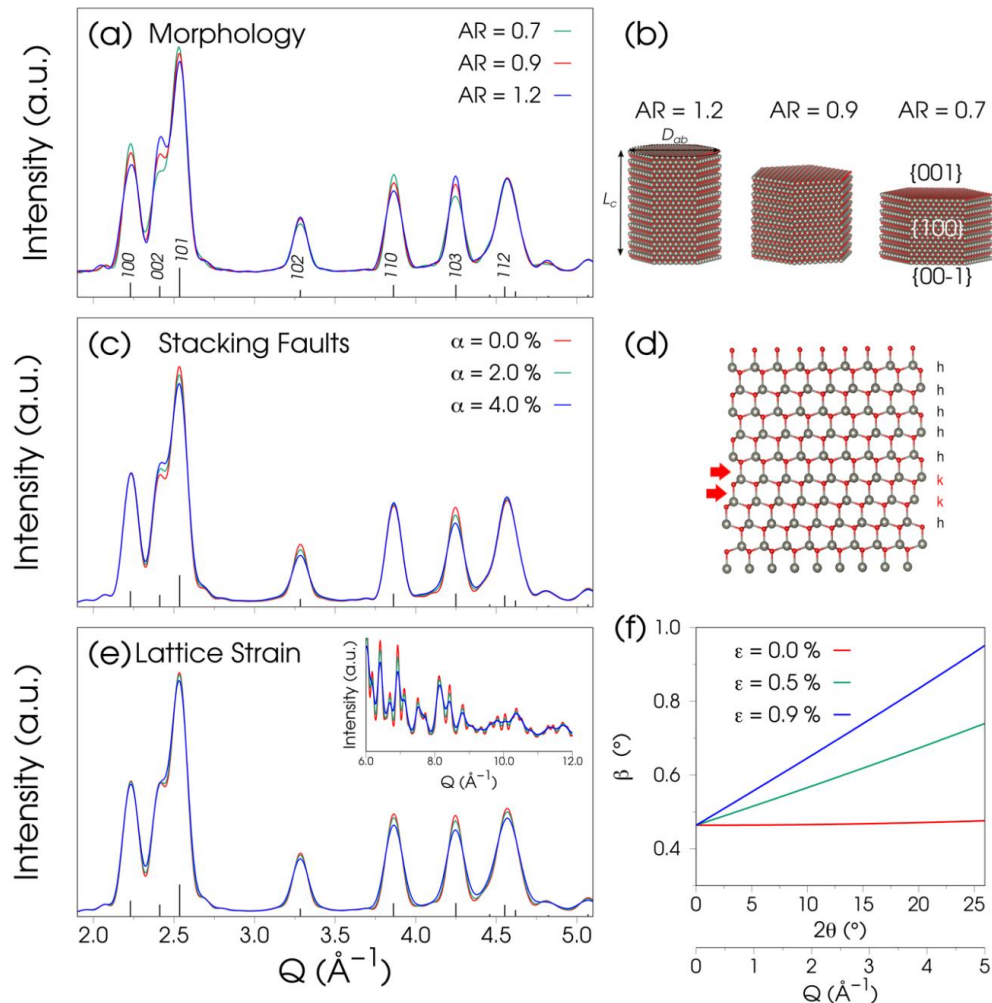


**Figure 1.** X-ray calculated patterns of ZnO NCs illustrating different correlated sources of peak broadening. (a, b) Anisotropic morphology of hexagonally shaped (defect-free) wurtzite ZnO NCs at increasing Aspect Ratio ( $AR = L_c/D_{ab}$ ), narrowing the  $002$  peak and concurrently widening the  $100$  and  $110$  peaks; (c) planar defects at increasing density  $\alpha$  of stacking faults, acting along specific  $(101, 102, 103)$  crystallographic directions; d) schematics of cubic plane defects ( $k$ ) breaking the regular wurtzite stacking ( $h$ ) of Zn (grey) and O (red) alternating layers along the  $[001]$  axis. Larger  $\alpha$  values do not modify the intensity of the  $100$  and  $110$  reflections that are strongly affected by morphology; e) isotropic lattice strain broadening particularly effective in the high  $Q$  region; f) integral breadth ( $\beta$ ) vs  $2\theta$  showing the angle-dependence at different strain parameter values  $\epsilon$  jointly to the finite-size component. All patterns are calculated using nearly equal volume NCs ( $125 \text{ nm}^3$ ) and  $AR = 0.9$  in (c,e).

### 3. RESULTS AND DISCUSSION

**X-ray fingerprinting of morphology and stacking faults in ZnO NCs.** VTMS-grafting has been reported to have a great control over ZnO nanoparticle size. Upon increasing the amount of silane, nearly spherical particles a few nanometres wide have been imaged (Figure S1). At this very small size, control over the NCs morphology remains poorly

investigated, partially due to aggregation phenomena limiting the analysis through imaging techniques. Even more difficult, under these circumstances, is the direct visualization (and quantification) of planar defects. In this work, we were interested in quantitatively extracting a number of structural and microstructural properties from WAXTS experiments performed on VTMS-grafted ZnO NCs, using the DSE

method of analysis. To this aim, a comprehensive atomistic model for ZnO NCs was developed (see Figure 1), jointly encoding: *i*) the wurtzite crystal structure with basal-plane defects breaking the regular hexagonal sequence, *ii*) the  $D_{6h}$  prismatic morphology with independent sizes along the  $c$  axis ( $L_c$ ) and in the  $ab$  plane ( $D_{ab}$ , the diameter of the circle of equivalent area to the hexagonal base) and *iii*) additional size/surface-driven lattice strain.

Since these structural features may have severe overlapping effects in the X-ray pattern of 5 nm ZnO NCs, we separately illustrate in Figure 1 their fingerprinting features by means of DSE calculated patterns (in the  $2.0 - 5.0 \text{ \AA}^{-1} Q$  range) from well-controlled ZnO atomistic models, as an exploratory step to the complex analysis of the experimental data. All calculations refer to equal volume models (ca.  $125 \text{ nm}^3$ ) leading to signals on the same scale, the size of which is in line with the smallest VTMS-grafted particles of this work.

In Figure 1a we used hexagonally shaped, ideal (defect-free) wurtzite ZnO NCs described by the  $L_c, D_{ab}$  pairs, to show the effects related to the anisotropic morphology. Slightly different (strictly monodisperse) NC sizes in Figure 1b, sampled at about 1 nm along the  $c$  axis and 0.6 nm in the  $ab$  plane ( $L_c = 6.26, 5.21$  and  $4.17 \text{ nm}$ ,  $D_{ab} = 5.03, 5.62$  and  $6.21 \text{ nm}$ , from left to right) are chosen to verify the DSE capability to capture even tiny Aspect Ratio ( $AR = L_c/D_{ab}$ ) variations, from 0.7 to 1.2. Detectable changes of Bragg peak widths are observed, dependent on the crystallographic direction. Upon increasing  $AR$ , the  $002$  and (to some extent)  $103$  peaks (carrying information on the coherent domain size along the  $c$  axis), progressively get narrower while the  $100, 101$  and  $110$  peaks simultaneously widen (due to the NCs domain extension in the orthogonal  $ab$  plane). These peculiar features are typically smeared out by size dispersions in real samples, a non-negligible effect in synthetic methods lacking a strict control of nucleation rates and crystal growth conditions.

The previous calculations are particularly useful in view of disentangling morphological and planar defect effects, as illustrated in Figure 1c-d. Figure 1d exemplifies the case of a single mistake in the regular wurtzite stacking ( $h$ ) introduced by double cubic ( $kk$ ) layers randomly located along the  $[001]$  axis (Pandey's  $h$  and  $k$  notation is adopted for sequence identification).<sup>68</sup> Details of the atomistic model construction of faulted ZnO sequences and computational issues for the DSE calculations are provided in the Experimental Section. Based on experimental evidence and previous considerations about the SF energy in ZnO, and in line with literature reports, SF densities ( $\alpha$ ) up to 6% were investigated within the model, meaning that few individuals are likely to be faulted within a large ensemble of unfaulted NCs of equal size. We applied the random probability model for the fault location in the sequence, according to Warren's theory.<sup>76</sup> Though such theory was developed for infinite sequence of layers, previous applications to CdSe zinc-blende

quantum dots (based on atomistic models and DSE analysis) demonstrated the validity also at the nanoscale for intrinsic SFs.<sup>59</sup>

According to the random approach, any fault location in the ZnO sequence has the same probability to take place, which (slightly) affects the X-ray pattern calculation. All possible configurations were therefore considered (within the reduced NCs length of 20 – 25 layers) and, to account for the "low" density of SFs, they were further "diluted" by a large number of unfaulted sequences of equal size, leading to the average DSE calculated pattern representative of each NC. According to this approach,  $\alpha$  counts the number of  $k$  layers over the total number ( $h+k$ ) in faulted and unfaulted NCs of our model. The lateral NCs size has no influence on the  $\alpha$  value, due to the equal extension of faulted and unfaulted planes.

Figure 1c shows the DSE simulations in NCs with  $AR = 0.9$  (see Figure 1b) at  $\alpha = 2\%$  and  $\alpha = 4\%$ , in comparison to the unfaulted case ( $\alpha = 0$ ). We notice that  $100, 002, 110$  and  $112$  peaks ( $hk0$  or  $hkl$  with  $l = 2n$  and  $h-k = 3n$ ) are substantially unaffected by the fault, whereas the  $101, 102$  and  $103$  peaks broaden upon increasing  $\alpha$ , in line with Langford *et al.*<sup>45</sup> and Wilson's rules<sup>77</sup> derived for ZnO and *hcp* metals, respectively. No angular shift of Bragg peaks is observed (as predicted by Warren's theory in *hcp* crystals<sup>76</sup>), meaning that SF information is confined in peak broadening only (in contrast to the *fcc* structure).<sup>45,76</sup> These observations also suggest possible correlations between  $\alpha$  and  $L_c$  NC size that must be taken into account in the data analysis. Worth to note, similar broadening effects are obtained when growth faults (single  $k$  layer) are considered, as demonstrated in Figure S2.

Figure 1e-f displays an additional source of peak broadening appearing in the VTMS-grafted ZnO WAXTS data. Linked to lattice (micro)strain, it indicates a distribution of the lattice periodicity about an average value within the sample. Considering the small NC sizes of the present work, we reasonably attribute the origin of the (micro)strain to surface-driven effects due to the VTMS grafting. We show in Figure 1e, isotropic strain broadening (within a Gaussian approximation) particularly effective in the high  $Q$  region, controlled by the adimensional parameter  $\varepsilon = \langle \varepsilon_i^2 \rangle^{1/2}$  ( $\varepsilon_i$  being the relative radial inflation/deflation of the lattice for the  $i$ -th crystal within the sample).<sup>78-80</sup> The angular dependence is graphically displayed as a continuous curve of the peak integral breadth ( $\beta$ ) vs  $2\theta$  (Figure 1e) at  $\varepsilon = 0.5\%$  and  $0.9\%$  (values suggested by the experimental data analysis). The strain-free curve, calculated for an equal average crystal size as that of previous DSE simulations, is provided for comparison. Worth of note is the strain influence on Bragg peak tails, possibly hindering evaluation of size dispersion effects.

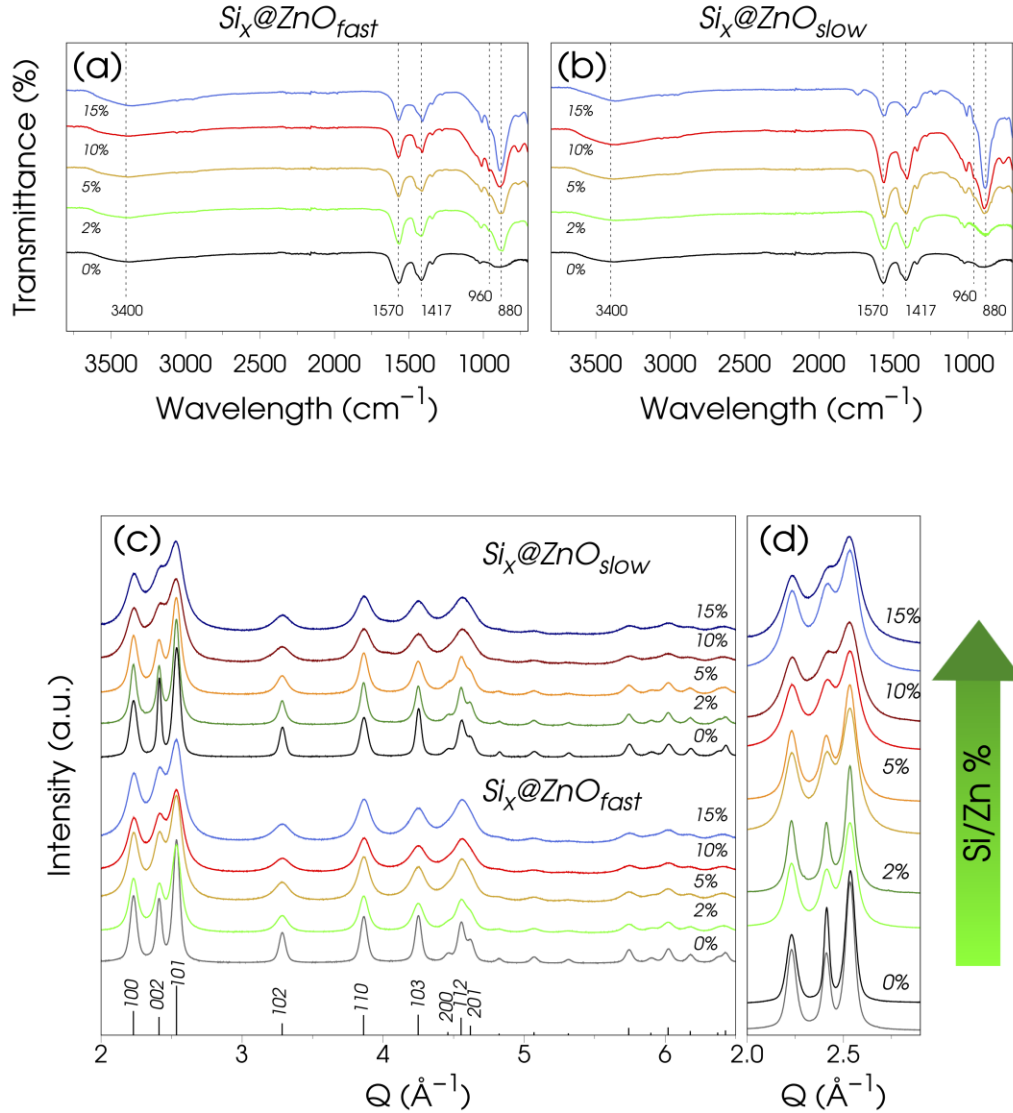


**Figure 2.** FTIR spectra and synchrotron X-ray data of unmodified and VTMS-grafted ZnO nanoparticles measured on  $\text{Si}_x\text{@ZnO}_{\text{fast}}$  and  $\text{Si}_x\text{@ZnO}_{\text{slow}}$  samples at increasing organosilane content ( $x = \text{Si/Zn}$  molar ratio, in the 0 – 15% range). a,b): the wide band centred at  $3400\text{ cm}^{-1}$  is assigned to the stretching mode of -OH groups. Two intense peaks at  $1570\text{ cm}^{-1}$  and  $1417\text{ cm}^{-1}$  are ascribed to the asymmetric and symmetric stretching modes of residue acetate groups. FTIR spectra of the VTMS-capped ZnO samples show two additional bands at  $960\text{ cm}^{-1}$  and  $880\text{ cm}^{-1}$  attributed to Zn-O-Si Si-O(H) and symmetric Si-O-Si symmetric stretching vibrations, respectively (further details are given in the Experimental Section). c) Wide-angle X-ray pattern sequences showing peak broadening upon Si/Zn increase. d) Blow-up of the 100, 002 and 101 peaks in the low-Q region for  $\text{Si}_x\text{@ZnO}_{\text{fast}}$  and  $\text{Si}_x\text{@ZnO}_{\text{slow}}$  pairs. At  $\text{Si/Zn} \geq 10\%$ , Bragg peaks become wider in the fast than in the slow series. Signals are shifted upwards for sake of clarity.

As later discussed, if neglected or poorly estimated, strain broadening can lead to biased average size and distribution parameters, whereas it has a minor direct influence on SF density determination.

**Spectroscopic and WAXTS preliminary analyses.** VTMS-grafted ZnO NCs were prepared by slightly modifying a reported synthetic method, where silane is present in the reaction solution during the NCs growth (see Experimental Section for details).<sup>33</sup> Two distinct series of specimens were isolated, corresponding to a rapid ( $\text{Si}_x\text{@ZnO}_{\text{fast}}$ ) and slow ( $\text{Si}_x\text{@ZnO}_{\text{slow}}$ ) crystallization process from the same initial solution, at variable Si/Zn molar ratios ( $x = 0, 2, 5, 10, 15\%$ ).

FTIR spectra are shown in Figure 2a-b for unmodified and silane-modified ZnO NCs. The two intense peaks at  $1570\text{ cm}^{-1}$  and  $1417\text{ cm}^{-1}$  appearing in all samples are ascribed to the asymmetric and symmetric stretching modes of -COO- moieties of residual acetate groups, not completely removed after the washing procedure. The appearance of two additional bands at  $960\text{ cm}^{-1}$  and  $880\text{ cm}^{-1}$  indicates the formation of Si-O(H) from partially hydrolysed VTMS and Si-O-Si bridges around the ZnO core, respectively, the latter confirming that condensation between the methoxy groups of VTMS and the hydroxyl groups from ZnO surface took place in both series.<sup>26,69,71</sup> A parallel rise of the intensity of



these new bands is observed in the two series upon increasing the silane amount, though rather weak in  $\text{Si}_x\text{@ZnO}_{\text{slow}}$  for  $x \leq 5\%$ . These findings suggest that a very minor amount of silane is also bound to ZnO in the slowly precipitated samples at these Si/Zn molar ratios.

WAXTS data, collected on the dry nanopowders, are shown in Figure 2c. Upon increasing the silane amount, Bragg peaks broaden indicating the successful isolation of progressively smaller ZnO NCs in both series (Figure 2c), apparently without any substantial difference between the two. However, the blow-up of homologous data in Figure 2d (in the significant  $2 - 3 \text{ \AA}^{-1} Q$  region) shows broader peaks in  $\text{Si}_x\text{@ZnO}_{\text{slow}}$  above 5% Si/Zn ratio, in agreement with IR spectral changes. As briefly discussed in the previous section, X-ray peak broadening is caused by a combination of multiple effects, the interpretation of which was pursued on a quantitative model basis. To this aim, a sophisticated X-ray total scattering pattern model was built, avoiding (as much as possible) phenomenological components and taking care of possible parameter correlation issues during the analysis, as detailed in the next section.

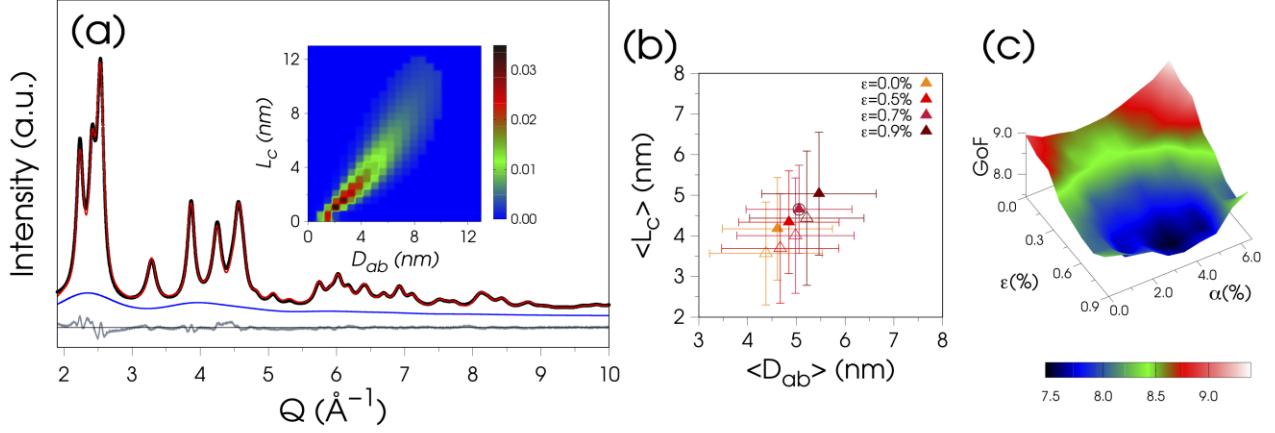
**A comprehensive DSE-based model of ZnO nanocrystals.** Hexagonal ( $D_{6h}$ ) prismatic NCs (as those shown in Figure 1b) were generated according to a discrete bivariate population where each NC is univocally identified by the  $L_c$ ,  $D_{ab}$  pairs. Faulted NCs were obtained by inserting double- $k$  basal deformations (intrinsic SFs) in the wurtzite sequence, as illustrated in Figure 1d. All these features were encoded as sampled interatomic distances and stored in suitable databases for the subsequent WAXTS data analysis using the *Debussy Suite*<sup>65</sup> (see the Experimental Section for details). The deformation fault was selected (among other possible options, such as growth and extrinsic faults) also in agreement with DFT calculations reporting that this kind of planar defects affects the conduction and valence bands of bulk ZnO eventually resulting in the band gap narrowing.<sup>49</sup> The occurrence of organosilanes bound to the ZnO surface was neglected in the model for two main reasons: 1) the structurally disordered and swinging silanes coating the ZnO core are expected to weakly contribute to the X-ray pattern with an amorphous-like halo; 2) such disordered silane outer layer is difficult to model within a population of NCs. WAXTS data analysis relied on an iterative procedure where the DSE calculated pattern is optimized against the experimental one, based on the Simplex method and standard  $\chi^2$  minimization.<sup>67</sup> A total of seven parameters were adjusted for the NCs population of each sample. These include pairs of average size and standard deviation ( $L_c$ ,  $\sigma_c$ ), ( $D_{ab}$ ,  $\sigma_{ab}$ ) along the two NCs growth directions according to a bivariate lognormal distribution function, the inclination angle  $\phi$  of the size-distribution map (elliptical in the log-log scale), and the isotropic atomic thermal displacements  $B_{\text{Zn}}$  and  $B_{\text{O}}$  (in the form of Debye-Waller  $B$ -factor). Once relaxed, oxygen vacancies never deviated from unity and, therefore, were fixed to 1 during the final model optimization. The fitting procedure is here exemplified for the VTMS-grafted ZnO NCs at the maximum Si/Zn ratio ( $\text{Si}_{15}\text{@ZnO}_{\text{fast}}$  and  $\text{Si}_{15}\text{@ZnO}_{\text{slow}}$ ), bearing the smallest size and the highest defects concentration. Figure 3a-d shows the corresponding best fits, which are gathered in the Supporting Information (Figure S3) for the other samples. The size distribution function is graphically represented in the insets of Figure

3a-d as a two-dimensional (2D) map in the ( $D_{ab}$ ,  $L_c$ ) coordinates, where the mass-based fraction of each NC within the population is given in colour code. Average NCs length ( $\langle L_c \rangle$ ) and cross section ( $\langle D_{ab} \rangle$ ) are calculated from projections onto the corresponding axis; the correlation coefficient (from the variance-covariance matrix) measures the possible correlations between growth axes.<sup>81</sup> Size-related values for unmodified and silane-modified samples are collected in Table S1 and Table S2. Their dependence on the Si/Zn ratio is later discussed, jointly to the other model parameters.

**Exploring fault density and lattice strain.** The two-steps approach used for the database generation and data analysis is a key point for speeding up the calculations, however it discourages the iteration on those parameters that modify the set of interatomic distances, requiring cyclic database restoration (unaffordable in terms of computational time). These include the SF density  $\alpha$  and the lattice strain  $\epsilon$  parameters. Taking into consideration also parameter correlation issues, optimization of  $\alpha$  and  $\epsilon$  was tackled through a grid search approach exploring the Goodness of Fit ( $\text{GoF} = \sqrt{\chi^2}$ ) statistical descriptor vs  $\alpha$  and  $\epsilon$  at the nodes of a 2D grid, in a model where all other (size and structural) parameters were relaxed (Figure 3c-f). Distinct databases were generated for each SF density, whereas the strain broadening was accounted for through a convolution approach. In the samples with the smallest particles (at Si/Zn molar ratios  $\geq 10\%$ ) the two-dimensional exploration spanned the  $\alpha$  values in the 0.0 – 6.0% range, in 0.5% steps, and the  $\epsilon$  values in the 0.0 – 0.9% range, in 0.15% steps. Though relatively shallow, distinct minima are noticeable at  $\alpha = 4.0\%$  in  $\text{Si}_{15}\text{@ZnO}_{\text{fast}}$  (Figure 3c),  $\alpha = 2.0\%$  in  $\text{Si}_{15}\text{@ZnO}_{\text{slow}}$  (Figure 3f) and  $\epsilon = 0.7\%$  in both samples, eventually suggesting a role of the NCs growth mode in the SF density at nearly comparable sizes. The best  $\alpha$  and  $\epsilon$  values of each sample (collected in Table S3) are discussed jointly to size and morphological parameters, in relation to the optical band gap energy variations upon changing the Si/Zn ratio. With reference to the size-strain parameter correlation issues, effects on the average NCs length  $\langle L_c \rangle$  vs  $\langle D_{ab} \rangle$  are exemplified in Figure 3b-e, which show the NCs sizes for the different  $\epsilon$  values at the best  $\alpha$  of each sample (from Figure 3c-f). Larger sizes (both  $\langle L_c \rangle$  and  $\langle D_{ab} \rangle$ ) are obtained at progressively larger  $\epsilon$  values, likely balancing the increased strain broadening. Deviations as large as 1 nm were obtained, whereas their standard deviations  $\sigma_c$  and  $\sigma_{ab}$  (the vertical and horizontal bars in Figure 3b-e) undergo minor changes, preserving the relative size dispersion of the samples.

**Experimental evidence of  $[\text{Zn}_{10}\text{O}_4(\text{OH})_{12}(\text{H}_2\text{O})_4]$  - super-tetrahedron clusters.** An additional model component of the DSE fits shown in Figure 3a-d needs to be elucidated. The DSE signal calculated from the ZnO NCs population was able to account for the total measured sample scattering only in the case of the unmodified materials, whereas some residual intensity resembling that of an amorphous-like phase remained unaccounted in all silane-modified samples. To clarify the nature of this component, an exploratory fit was performed of the  $\text{Si}_{15}\text{@ZnO}_{\text{slow}}$  data, where the extra scattering was modelled using a polynomial function. The pair distribution function in the form of

# $Si_{15}@ZnO_{fast}$



# $Si_{15}@ZnO_{slow}$

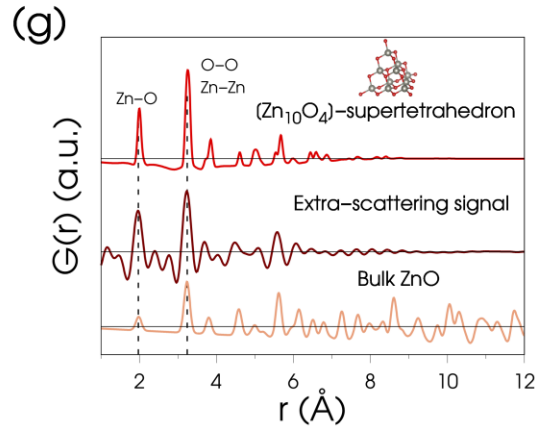
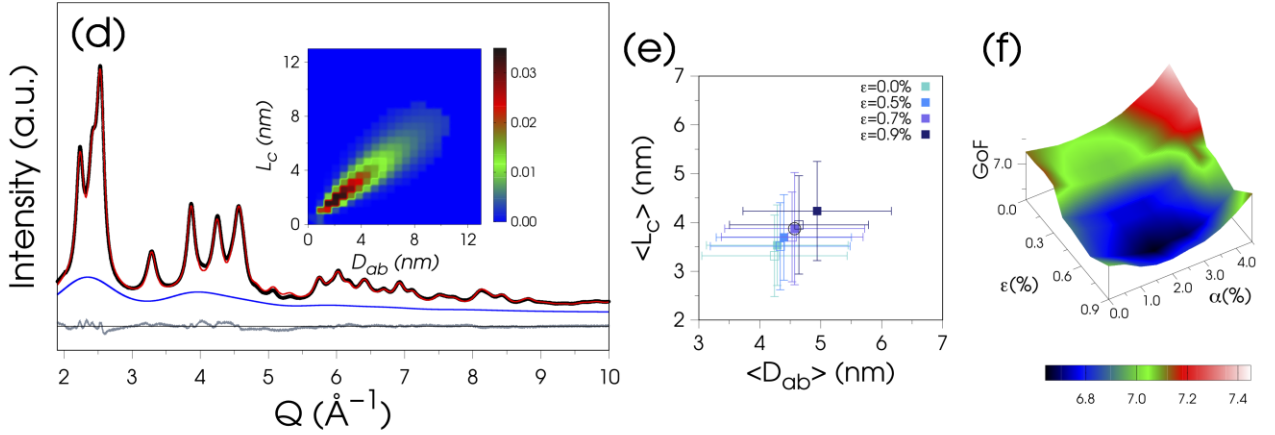


**Figure 3.** DSE analysis of  $Si_{15}@ZnO_{fast}$  and  $Si_{15}@ZnO_{slow}$  NCs. (a, d) X-ray synchrotron data (black dots), DSE best fit resulting from the NCs population (red pattern) jointly to an amorphous-like component (blue curve), and residual trace (gray). Insets: 2D map of the bivariate lognormal size distribution of the ZnO NCs. Each pixel in the map provides the NC size (length,  $L_c$ , and diameter,  $D_{ab}$ ) and its mass fraction (in color scale) within the population. (b, e) Size-strain correlation plots showing that larger average sizes are obtained at progressively larger  $\epsilon$  values. The minimum GoF at  $\epsilon = 0.7\%$  for both  $Si_x@ZnO_{fast}$  and  $Si_x@ZnO_{slow}$  is highlighted (circled symbols). (c, f) 3D plots of GoF vs microstrain ( $\epsilon$ ) and stacking fault density ( $\alpha$ ). The minimum GoF is found at  $\alpha = 4.0\%$ ,  $\epsilon = 0.7\%$  in  $Si_x@ZnO_{fast}$  and  $\alpha = 2.0\%$ ,  $\epsilon = 0.7\%$  in  $Si_x@ZnO_{slow}$ . (g)  $G(r)$  curves corresponding to bulk ZnO (orange curve), the extra-scattering in  $Si_{15}@ZnO_{slow}$  (brown) and the  $[Zn_{10}O_4]$ -supertetrahedron (red).



$G(r)$ , obtained by Fourier transforming this “background” term, is shown in Figure 3g.<sup>82</sup> The shortest distances are assignable to Zn–O (1.97 Å) and Zn–Zn/O–O (3.25 Å), suggesting the occurrence of sub-nanometric ZnO clusters. The Si–O bond distance from the silane (expected as a weak peak at about 1.6 Å) cannot be clearly detected in the  $G(r)$ , likely hindered by truncation effects. Taking inspiration from the  $G(r)$  finding and from reported stable structures predicted to form during ZnO nucleation and growth,<sup>83,84</sup> a rigid  $[\text{Zn}_{10}\text{O}_4(\text{OH})_{12}(\text{H}_2\text{O})_4]$ -supertetrahedron cluster was built using geometrical considerations (inset of Figure 3g). The calculated  $G(r)$  of this cluster, also shown in Figure 3g, well matches the experimental one, further supporting our interpretation. Small clusters of this type are likely entrapped in the inter-voids between larger silane-coated ZnO particles and may further bind silane and acetate residues. The DSE calculated pattern of the supertetrahedron (the blue traces in Figure 3a-d) was added to the model and scaled to the experimental data, jointly to the signal from the nanocrystalline population. Scaling of this signal is likely affected by the presence of the organosilanes neglected in the DSE model. Quantification of the supertetrahedron cluster was obtained for each sample (see Table S3), as detailed in the Experimental section. Non-negligible amounts (in the 15-25 w% range) are found in all VTMS-grafted samples, peaking at nearly 38.5 w% in the  $\text{Si}_{15}@\text{ZnO}_{\text{slow}}$ .

**VTMS control over ZnO NCs size, morphology and fault density.** The dependence of size, morphology and SF density on the silane amount is discussed by means of Figure 4 for unmodified and VTMS-grafted ZnO NCs, also in relation to the different growth mode of the two series. DSE-derived (mass-based) average  $\langle L_c \rangle$  vs  $\langle D_{ab} \rangle$  values are shown in Figure 4a (fast growth) and Figure 4b (slow growth) at the different Si/Zn ratios, where horizontal and vertical bars are the standard deviations (see also Table S1). The NCs anisotropic morphology is measured by the average sample aspect ratio  $\langle AR \rangle = \langle L_c \rangle / \langle D_{ab} \rangle$  (Figure 4a-b). Throughout this paper we refer to mass-based averages that we consider more representative for polydisperse NCs characterized by X-ray scattering techniques. Number-based values are collected in Table S2. The diameter of the sphere of equivalent volume to the hexagonal prisms ( $\langle D_{eq} \rangle_M$  and  $\langle D_{eq} \rangle_N$ ) are also provided as a single measure of size.  $\langle D_{eq} \rangle_N$  are properly compared to TEM-based estimations in Table S2 (images available in Figure S1). As anticipated, inherent difficulties due to silane polymerization and partial NCs aggregation weakened the TEM analysis. This prevented any size dependence on the Si/Zn ratio to be detected and provided systematically larger sizes (jointly to unrealistic ul-

tranarrow size dispersions) than DSE-based ones (attributed to the nanocrystalline cores only, neglecting the silane coating).

The absence of silane results in larger ( $\langle D_{eq} \rangle_M$  in the 10-17 nm range) and prolated NCs ( $\langle AR \rangle > 1$ ) in the unmodified compounds, particularly elongated under slow growth conditions.

This observation is in line with a faster growth along the [001] axis and the fact that the basal {001} polar facets are energetically unfavoured.<sup>85–88</sup> First-principles calculations of the surface energy indicate a nearly halved value (2.2 vs 1.1 J/m<sup>2</sup>) of the non-polar lateral surfaces compared to the polar (001)-Zn ones, consistent with observations in ZnO nanostructures.<sup>89</sup> A similar consideration applies to  $\text{Si}_x@\text{ZnO}_{\text{slow}}$  at the lowest silane amounts ( $x \leq 5\%$ ) exhibiting  $\langle AR \rangle \sim 1$ . This finding suggests that VTMS is largely depleted through the first precipitation, in line with IR spectra and as further confirmed by the NCs size larger than in the  $\text{Si}_x@\text{ZnO}_{\text{fast}}$  series. A persistent  $\langle AR \rangle \sim 0.8\text{--}0.9$  is found in the remaining VTMS-grafted samples, where sizes shrink from 10 nm down to 4 nm at progressively higher silane amount. Their relative dispersions are within 43 – 50% for  $D_{ab}$ , slightly larger for  $L_c$  in  $\text{Si}_x@\text{ZnO}_{\text{fast}}$ , and about 50% for both directions in  $\text{Si}_x@\text{ZnO}_{\text{slow}}$ . No relevant size and morphological differences are observed between the two series under the action of comparable silane amounts ( $\text{Si}/\text{Zn} \geq 10\%$ ). These results indicate a superior control of VTMS over NCs size (though moderate for size dispersion) jointly to an excellent morphological control that limits the ZnO to grow along the [001] axis, leading to the conclusion that silane preferentially binds the polar basal facets. In order to investigate the dependence of the stacking fault density  $\alpha$  on the Si/Zn ratio, the DSE models were explored over a range of  $\alpha$  values for all VTMS-modified samples, similarly to what illustrated for the samples at the highest silane content (Figure 3). Plots of the GoF statistical indicator vs  $\alpha$  from this analysis are shown in Figure 4c for the  $\text{Si}_x@\text{ZnO}_{\text{fast}}$  NCs, and in Figure 4d for the  $\text{Si}_x@\text{ZnO}_{\text{slow}}$  ones. The SF density  $\alpha$  of each sample is taken from the minimum GoF of the corresponding curve. In  $\text{Si}_x@\text{ZnO}_{\text{fast}}$ , the value increases from  $\alpha = 1.5\%$  (at  $x = 2\%$ ) to  $\alpha = 4\%$  (at  $x = 15\%$ ), corresponding to  $0.6 \times 10^6$  and  $1.6 \times 10^6 \text{ cm}^{-1}$  linear densities, in line with HIM-based reported values.<sup>48</sup> In contrast,  $\alpha$  varies in the 1-2% range ( $0.4 \times 10^6 - 0.8 \times 10^6 \text{ cm}^{-1}$ ) in  $\text{Si}_x@\text{ZnO}_{\text{slow}}$ , where the much slower NCs growth likely favors self-healing of defects. These results indicate a higher density of planar defects in NCs grown in rapid mode and an inverse dependence of  $\alpha$  on the Si/Zn ratio (therefore, on size NCs) in both series, as documented in Figure 4c-d. A similar inverse size dependence of fault density was also found in CdSe quantum dots.<sup>59</sup>

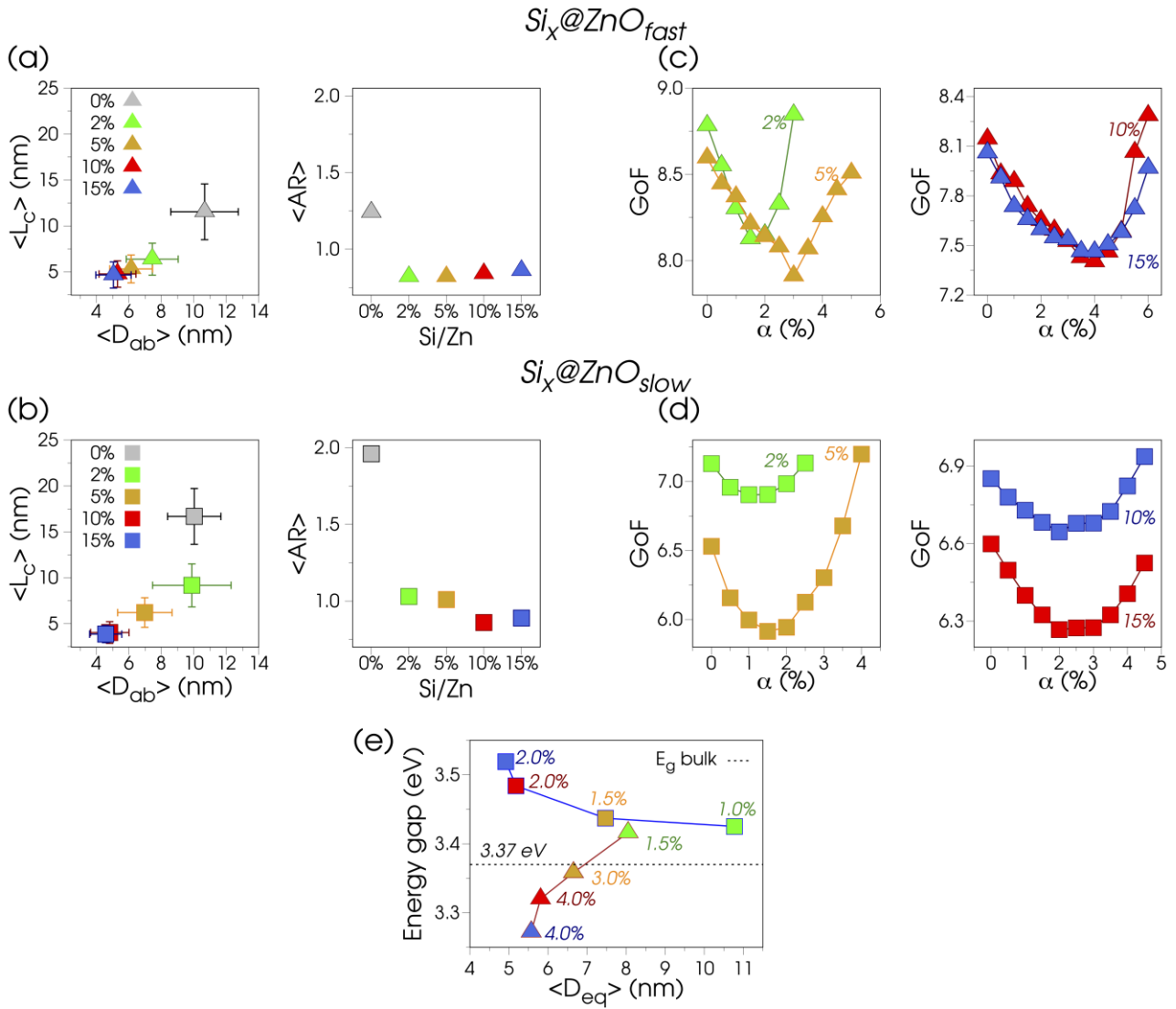


**Figure 4.** DSE-based results of the  $\text{Si}_x\text{@ZnO}_{\text{fast}}$  (triangles) and  $\text{Si}_x\text{@ZnO}_{\text{slow}}$  (squares) samples vs the Si/Zn molar ratio. (a, b) Average length  $L_c$  (parallel to the [001] wurtzite axis), diameter  $D_{ab}$  (of the circle of equivalent area in the  $ab$  plane) and Aspect Ratio ( $\langle AR \rangle = \langle L_c \rangle / \langle D_{ab} \rangle$ ), all referred to the NCs hexagonal morphology. Horizontal and vertical bars in a) are the standard deviations ( $\sigma_{ab}$  and  $\sigma_c$ ) of the bivariate lognormal distribution measuring the size dispersion in the two directions. (c, d) GoF of the DSE fits vs stacking fault density  $\alpha$ . (e) Optical band gap energy vs  $\langle D_{eq} \rangle$  (the diameter of the sphere of equivalent volume to the hexagonal prisms), for  $\text{Si}_x\text{@ZnO}_{\text{fast}}$  (triangles) and  $\text{Si}_x\text{@ZnO}_{\text{slow}}$  (squares).

**Optical band gap energy dependence on NCs size and density of planar defects.** The energy band gap ( $E_g$ ) of unmodified and silane-modified ZnO NCs was determined from UV-vis transmittance spectra using Tauc plots (Figure S4). We analysed  $E_g$  as a function of NCs size for the two series in Figure 4e, taking  $\langle D_{eq} \rangle$  as a single size measure. Significantly, results do not change if number-based averages (smaller by a factor  $\sim 3$ ) are considered. In agreement with the quantum confinement effect (the exciton diameter in ZnO  $\approx 2$  nm<sup>43</sup>),  $\text{Si}_x\text{@ZnO}_{\text{slow}}$  NCs exhibit the expected inverse size dependence of the optical band gap, with  $E_g$  rising by 0.15 eV from the reference bulk 3.37 eV value, at  $\langle D_{eq} \rangle = 4.9$  nm. In contrast,  $\text{Si}_x\text{@ZnO}_{\text{fast}}$  NCs exhibit an unexpected  $E_g$  decrease down to 3.27 eV at the smallest  $\langle D_{eq} \rangle$  of 5.0 nm. In search for plausible causes, differences on NCs morphology (that have been reported to influence the ZnO band gap)<sup>7</sup>

are here discarded based on the results of the DSE analysis providing nearly equal  $\langle AR \rangle \approx 0.9$  for the two series at the smallest sizes (Figure 4a and 4b). Likewise, electronic influence from silanes is not able to explain the finding, as it is expected to affect the optical band gap of the two series in a nearly similar way.

To elucidate the opposite behavior for the two series upon downsizing, planar defects and lattice relaxation and their correlation with  $E_g$  have been investigated. SF density  $\alpha$  values provided by the DSE analysis are displayed in Figure 4e for each sample showing their inverse size dependence. As previously commented, the density of SFs shows striking differences between the two series, which are well explained by the different NCs growth rate, the largest densities being observed in  $\text{Si}_x\text{@ZnO}_{\text{fast}}$  samples. First-principles density-functional energy calculations by Yan et al. indicated that planar [001] SFs have low formation energy (55

mJ m<sup>-2</sup>).<sup>49</sup> In their paper, the authors suggested that, where SFs form in high concentration, they result in zincblende (ZB) domains embedded within the wurtzite (WZ) structure; the conduction band in faulted structures is reported

to be 20 to 40 meV lower (depending on the type of fault) than in perfect crystals.

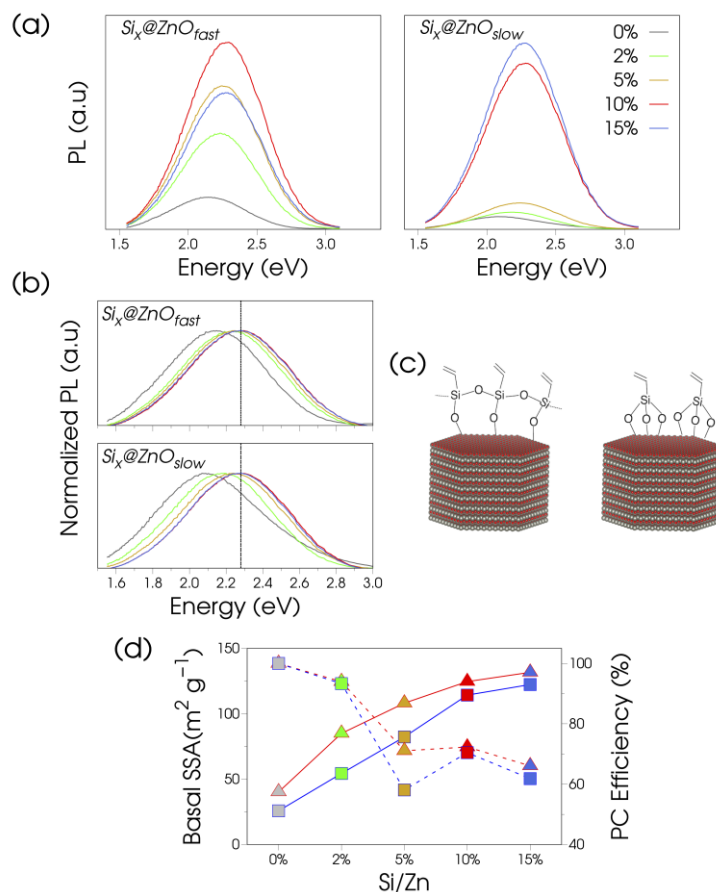


**Figure 5.** (a) Photoluminescence (PL) spectra of  $\text{Si}_x\text{@ZnO}_{\text{fast}}$  and  $\text{Si}_x\text{@ZnO}_{\text{slow}}$  samples at increasing Si/Zn ratio. (b) PL spectra as in (a) normalized to the same maximum intensity. (c) Sketch of monodentate and tridentate silane bonding to the surface of ZnO NCs. (d) Basal SSA of  $\text{Si}_x\text{@ZnO}_{\text{fast}}$  (triangles) and  $\text{Si}_x\text{@ZnO}_{\text{slow}}$  (squares) (symbols connected by the solid lines) and photocatalytic (PC) efficiency (symbols connected by the dashed lines) vs Si/Zn ratio.

For deformation faults, the band alignment at the WZ/ZB/WZ regions exhibits quantum-well features and carrier localization; calculations indicate that WZ band gap is 0.11 eV larger than that in ZB ZnO. Though additional confinement effects might be present by NCs downsizing, these DFT calculations support the observed decrease by 0.10 eV from the bulk value at the largest SF densities. Qualitatively similar results, based on theoretical calculations of the DFT type for a number of II-VI and III-V semiconductors, have been reported.<sup>49,90</sup>

Lattice deformations upon the NCs size decrease were also analysed, either as macrostrain (that is the cell expansion, measured by the relative variations  $\Delta a/a_0$ ,  $\Delta c/c_0$ ,  $a_0$  and  $c_0$  being the reference bulk parameters) shown in Figure S5, or as microstrain (the  $\epsilon$  parameters, reported in Table S3). Modest macrostrain values below 0.2% are observed:  $\Delta a/a_0$  exhibits a nearly constant 0.12% value,  $\Delta c/c_0$  an inverse size dependence and values in the 0.05 – 0.19% range. Though

possibly influencing the band gap, differences are not observed between the two silane-grafted ZnO series to justify the opposite  $E_g$  behaviour with the NCs size. With reference to the microstrain, values fall in the 0.2 – 0.7 % range in both series, the smallest  $\epsilon$  values being found at  $\text{Si/Zn} \leq 5\%$ . This finding points to a surface-driven effect and to a parallel  $\epsilon$  dependence on the amount of silane in both  $\text{Si}_x\text{@ZnO}_{\text{fast}}$  and  $\text{Si}_x\text{@ZnO}_{\text{slow}}$  series.

Finally, other kind of defects such as dislocations cannot be fully disregarded as possible origin of the observed trends in optical bandgap. Indeed, dislocation-related emission bands are reported in single crystals (at 3.1 eV, lower than the bulk ZnO bandgap, but also at the higher energy of 3.45 eV), upon material deformation at elevated temperatures introducing point like oxygen vacancies inside the core structure.<sup>91</sup> However, in contrast to those formed at high temperatures, dislocations introduced at room temperature are reported to act as non-radiative centres. Therefore, a specific role of dislocations is unlikely to take place in the

emission properties of the ZnO samples investigated in the present work.

**Visible emission and photocatalytic properties vs VTMS surface coating.** The green emission of ZnO has been a controversial subject for long time and still is a matter of investigation. It is typically attributed to point defects (vacancies and interstitial atoms), though with contradictory assignment of sites and possible sources of the deep trap states.<sup>41</sup> In small nanoparticles, point defects are thought to be mainly located on their surfaces and visible luminescence is reported to be strongly dependent on passivation of oxygen vacancies.<sup>31</sup> In line with these considerations and with previous reports, the VTMS-grafted ZnO NCs presented in this work exhibit a remarkable enhancement of the visible photoluminescence (PL) in comparison to their unmodified counterparts, particularly evident at the highest Si/Zn ratios ( $\geq 10\%$ ) (Figure 5a). Further supported by the FTIR spectra discussed in Figure 2a-b, these observations corroborate the relation between silane grafting, passivation of oxygen vacancies at the surface and PL enhancement.<sup>28,29</sup>

The analysis of the PL spectra, normalized to the maximum intensity in Figure 5b, further highlights that the emission peak is blue shifted in comparison to that of unmodified materials. Shifts are larger in the  $\text{Si}_x\text{@ZnO}_{\text{slow}}$  than in the  $\text{Si}_x\text{@ZnO}_{\text{fast}}$  series, in line with the wider band gap of the former and the recombination at deep localized states related to the visible emission. This finding points to the (often disregarded) influence of planar defects in the green luminescence of ZnO NCs. However, at Si/Zn ratio  $\geq 10\%$ , all samples show the emissive band peaking at 2.30 eV, in both series, without any additional shifts. In this regard, the silane-ZnO surface interactions at the different silane amounts may lead to a reasonable interpretation. As elucidated by <sup>29</sup>Si and <sup>13</sup>C solid state NMR studies<sup>34</sup> of ZnO nanoparticles prepared by the same synthetic route as in the present work, the Si atoms may bind to the ZnO surface by three, two or one oxygen bridge(s) (as depicted in Figure 5c for the first and last cases), the amounts of the different bonding types depending on the silane concentration.<sup>33</sup>

At the largest Si/Zn ratio of 10% in ref. <sup>33</sup>, the formation of an inner layer bound to the ZnO surface and an outer shell consisting of a three-dimensional Si-O-Si network, without Zn-O-Si links, was suggested, favoured by monodentate bonding.<sup>33</sup> Accordingly, a (previously reported)<sup>29</sup> donor effect of silanes influencing the ZnO band gap should be considered in relation to the concentration of the different bonding types. At the largest amounts of silane of the present work, the observed photoluminescence peaks at 2.30 eV might be the consequence of the saturation of VTMS molecules grafted at the NCs surface, with comparable concentrations of silane bonding types in both ZnO series.

We further investigated the organosilane coating around the inorganic ZnO core by performing methylene blue degradation experiments (Figure S6), taking advantage of the remarkable photocatalytic activity of ZnO NCs favoured by the combination of electronic and surface properties.<sup>5,39</sup> The morphological results of the DSE-based analysis suggested the preferential binding of VTMS to the basal {001} facets of ZnO NCs. These are also reported to be the most active in photocatalytic reactions.<sup>85,88,92,93</sup> In line with this considera-

tion, the presence of the VTMS coating degrades the photocatalytic (PC) efficiency in the silane-modified ZnO particles.

To further elucidate the role of basal facets in the presence of grafting molecules, the corresponding specific surface area (basal SSA) was calculated from the DSE model of unmodified and silane-modified NCs (solid lines connecting symbols in Figure 5d) and used for a comparable analysis of the PC efficiency at increasing silane amount (dashed lines connecting symbols in Figure 5d and Table S4). Despite of their smallest basal SSA, the unmodified NCs of the two series showed both the highest PC efficiency and the ability of a full methylene degradation after 1h of exposure. A small amount of silane slightly lowers the efficiency to 93%. At larger amounts, a comparable PC efficiency reduction is found for the two series, and a more rapid rise of the basal SSA curve at low Si/Zn ratio is observed in the  $\text{Si}_x\text{@ZnO}_{\text{fast}}$  series (depleting the amount of VTMS in the  $\text{Si}_x\text{@ZnO}_{\text{slow}}$  series). Worth to note, a remarkable efficiency as high as 60% of that of the unmodified material is still measured, suggesting that the structure of the VTMS residues may form an inhomogeneous porous shell around the NCs, and that active sites may remain accessible to the organic dyes even at the highest silane coverage.

#### 4. CONCLUSIONS

Two series of nanosized ZnO powders bearing covalently grafted vinyltrimethoxysilane molecules were precipitated at increasing Si/Zn molar ratios upon fast and slow NCs growth, and thoroughly characterized by advanced X-ray total scattering synchrotron techniques, atomistic models of nanocrystals encoded in a bivariate population of anisotropically-shaped, defective individuals and the reciprocal space-based DSE method. A comprehensive picture of structural and morphological properties and crystal defectiveness (strain and stacking faults along [001]) of VTMS-grafted ZnO NCs is provided, jointly to experimental evidence of the occurrence of  $[\text{Zn}_{10}\text{O}_4(\text{OH})_{12}(\text{H}_2\text{O})_4]$ -supertetrahedron clusters predicted to form during ZnO nucleation and growth. We emphasize the challenging outcome of quantifying the SFs linear density in very small ZnO NCs, in the  $0.8 \times 10^6 - 1.6 \times 10^6 \text{ cm}^{-1}$  (1-4%) range, enabling unique correlations with electronic and optical properties. In particular, the unexpected band gap lowering upon downsizing, ca. 0.10 eV from the nominal value of the bulk, has been here interpreted by the presence of the large planar stacking faults density ( $1.6 \times 10^6 \text{ cm}^{-1}$ ) opposing to quantum confinement effects that control the band gap in NCs showing lower SF density ( $0.8 \times 10^6 \text{ cm}^{-1}$ ). Additional correlations between tiny shifts of the green-emission line and silane coverage, basal specific surface area and photocatalytic efficiency have been discussed. This work confirms that accurate synchrotron X-ray wide-angle scattering methods and tailored data analysis can provide a bevy of statistically robust structural and microstructural information on ultrasmall nanocrystalline materials.

## ASSOCIATED CONTENT

### Supporting Information

The Supporting Information is available free of charge on the ACS Publications website.

Additional information on the deformation fault density calculation, TEM images, DSE-best fits of all samples, Tauc plots for the band gap estimation, results of the methylene blue degradation experiments, tables quoting values of size and morphology from DSE analysis (PDF file).

## AUTHOR INFORMATION

### Corresponding Author

antonella.guagliardi@ic.cnr.it  
norberto.masciocchi@uninsubria.it  
aurel.tabacaru@ugal.ro

### Author Contributions

The manuscript was written through contributions of all authors.

### Funding Sources

This work was partially funded by MIUR (PRIN-2017L8WW48, Project HY-TEC).

## ACKNOWLEDGMENT

We heartily acknowledge the assistance of the technical staff of the MS-X04SA beamline of SLS.

## REFERENCES

- (1) Tian, Z. R.; Voigt, J. A.; Liu, J.; McKenzie, B.; McDermott, M. J.; Rodriguez, M. A.; Konishi, H.; Xu, H. Complex and Oriented ZnO Nanostructures. *Nat. Mater.* **2003**, *2*, 821–826.
- (2) Özgür, Ü.; Alivov, Y. I.; Liu, C.; Teke, A.; Reshchikov, M. A.; Doğan, S.; Avrutin, V.; Cho, S. J.; Morkoç, H. A Comprehensive Review of ZnO Materials and Devices. *J. Appl. Phys.* **2005**, *98*, 041301.
- (3) Schmidt-Mende, L.; MacManus-Driscoll, J. L. ZnO – Nanostructures, Defects, and Devices. *Mater. Today* **2007**, *10*, 40–48.
- (4) Tsukazaki, A.; Ohtomo, A.; Onuma, T.; Ohtani, M.; Makino, T.; Sumiya, M.; Ohtani, K.; Chichibu, S. F.; Fuke, S.; Segawa, Y.; et al. Repeated Temperature Modulation Epitaxy for P-Type Doping and Light-Emitting Diode Based on ZnO. *Nat. Mater.* **2004**, *4*, 42–46.
- (5) Yang, J. L.; An, S. J.; Park, W.; Yi, G.-C.; Choi, W. Photocatalysis Using ZnO Thin Films And Nanoneedles Grown By Metal-Organic Chemical Vapour Deposition. *Adv. Mater.* **2004**, *16*, 1661–1664.
- (6) Ahn, M. W.; Park, K. S.; Heo, J. H.; Park, J. G.; Kim, D. W.; Choi, K. J.; Lee, J. H.; Hong, S. H. Gas Sensing Properties of Defect-Controlled ZnO-Nanowire Gas Sensor. *Appl. Phys. Lett.* **2008**, *93*, 263103.
- (7) Bacsá, R. R.; Dexpert-Ghys, J.; Verelst, M.; Falqui, A.; Machado, B.; Bacsá, W. S.; Chen, P.; Zakeeruddin, S. M.; Graetzel, M.; Serp, P. Synthesis and Structure–Property Correlation in Shape-Controlled ZnO Nanoparticles Prepared by Chemical Vapor Synthesis and Their Application in Dye-Sensitized Solar Cells. *Adv. Funct. Mater.* **2009**, *19*, 875–886.
- (8) Huang, M. H.; Mao, S.; Feick, H.; Yan, H.; Wu, Y.; Kind, H.; Weber, E.; Russo, R.; Yang, P. Room-Temperature Ultraviolet Nanowire Nanolasers. *Science* **2001**, *292*, 1897–1899.
- (9) L. Qian; Y. Zheng; J. Xue; P. H. Holloway. Stable and Efficient Quantum-Dot Light-Emitting Diodes Based on Solution-Processed Multilayer Structures. *Nat. Photonics* **2011**, *5*, 543–548.
- (10) Khuong P. Ong; David J. Singh; Ping Wu. Analysis of the Thermoelectric Properties of N-Type ZnO. *Phys. Rev. B* **2011**, *83*, 115110–1–5.
- (11) Buonsanti, R.; Llordes, A.; Aloni, S.; Helms, B. A.; Milliron, D. J. Tunable Infrared Absorption and Visible Transparency of Colloidal Aluminum-Doped Zinc Oxide Nanocrystals. *Nano Lett.* **2011**, *11*, 4706–4710.
- (12) Liang, Z.; Zhang, Q.; Wiranwetchayan, O.; Xi, J.; Yang, Z.; Park, K.; Li, C.; Cao, G. Effects of the Morphology of a ZnO Buffer Layer on the Photovoltaic Performance of Inverted Polymer Solar Cells. *Adv. Funct. Mater.* **2012**, *22*, 2194–2201.
- (13) Della Gaspera, E.; Bersani, M.; Cittadini, M.; Guglielmi, M.; Pagani, D.; Noriega, R.; Mehra, S.; Salleo, A.; Martucci, A. Low-Temperature Processed Ga-Doped ZnO Coatings from Colloidal Inks. *J. Am. Chem. Soc.* **2013**, *135*, 3439–3448.
- (14) Della Gaspera, E.; Chesman, A. S. R.; van Embden, J.; Jasieniak, J. J. Non-Injection Synthesis of Doped Zinc Oxide Plasmonic Nanocrystals. *ACS Nano* **2014**, *8*, 9154–9163.
- (15) Li, S.; Sun, Z.; Li, R.; Dong, M.; Zhang, L.; Qi, W.; Zhang, X.; Wang, H. ZnO Nanocomposites Modified by Hydrophobic and Hydrophilic Silanes with Dramatically Enhanced Tunable Fluorescence and Aqueous Ultrastability toward Biological Imaging Applications. *Sci. Rep.* **2015**, *5*, 8475.
- (16) Khokhra, R.; Bharti, B.; Lee, H.-N.; Kumar, R. Visible and UV Photo-Detection in ZnO Nanostructured Thin Films via Simple Tuning of Solution Method. *Sci. Rep.* **2017**, *7*, 15032.
- (17) Spanhel, L.; Anderson, M. A. Semiconductor Clusters in the Sol-Gel Process: Quantized Aggregation, Gelation, and Crystal Growth in Concentrated Zinc Oxide Colloids. *J. Am. Chem. Soc.* **1991**, *113*, 2826–2833.
- (18) Liu, B.; Zeng, H. C. Hydrothermal Synthesis of ZnO Nanorods in the Diameter Regime of 50 Nm. *J. Am. Chem. Soc.* **2003**, *125*, 4430–4431.
- (19) Carcia, P. F.; McLean, R. S.; Reilly, M. H.; Nunes, G. Transparent ZnO Thin-Film Transistor Fabricated by Rf Magnetron Sputtering. *Appl. Phys. Lett.* **2003**, *82*, 1117–1119.
- (20) Polarz, S.; Roy, A.; Merz, M.; Halm, S.; Schröder, D.; Schneider, L.; Bacher, G.; Kruis, F. E.; Driess, M. Chemical Vapor Synthesis of Size-Selected Zinc Oxide Nanoparticles. *Small* **2005**, *1*, 540–552.
- (21) Jayawardena, K. D. G. I.; Fryar, J.; Silva, S. R. P.; Henley, S. J. Morphology Control of Zinc Oxide Nanocrystals via Hybrid Laser/Hydrothermal Synthesis. *J. Phys. Chem. C* **2010**, *114*, 12931–12937.
- (22) Søndergaard, M.; Bøjesen, E. D.; Christensen, M.; Iversen, B. B. Size and Morphology Dependence of ZnO Nanoparticles Synthesized by a Fast Continuous Flow Hydrothermal Method. *Cryst. Growth Des.* **2011**, *11*, 4027–4033.
- (23) Liu, Y.; Tai, K.; Dillon, S. J. Growth Kinetics and Morphological Evolution of ZnO Precipitated from Solution. *Chem. Mater.* **2013**, *25*, 2927–2933.
- (24) Laurenti, M.; Stassi, S.; Canavese, G.; Cauda, V. Surface Engineering of Nanostructured ZnO Surfaces. *Adv. Mater. Interfaces* **2017**, *4*, 1600758.
- (25) Wolska-Pietkiewicz, M.; Tokarska, K.; Wojewódzka, A.; Wójcik, K.; Chwojnowska, E.; Grzonka, J.; Cywiński, P. J.; Chudy, M.; Lewiński, J. ZnO Nanocrystals Derived from Organometallic Approach: Delineating the Role of Organic Ligand Shell on Physicochemical Properties and Nano-Specific Toxicity. *Sci. Rep.* **2019**, *9*, 18071.
- (26) Costenaro, D.; Carniato, F.; Gatti, G.; Marchese, L.; Bisio, C. Preparation of Luminescent ZnO Nanoparticles Modified with Aminopropyltriethoxy Silane for Optoelectronic Applications. *New J. Chem.* **2013**, *37*, 2103–2109.
- (27) Shi, H.-Q.; Li, W.-N.; Sun, L.-W.; Liu, Y.; Xiao, H.-M.; Fu, S.-Y. Synthesis of Silane Surface Modified ZnO Quantum Dots with Ultrastable, Strong and Tunable Luminescence. *Chem. Commun.* **2011**, *47*, 11921–11923.

- (28) Muşat, V.; Tăbăcaru, A.; Vasile, B. Ş.; Surdu, V.-A. Size-Dependent Photoluminescence of Zinc Oxide Quantum Dots through Organosilane Functionalization. *RSC Adv.* **2014**, *4*, 63128–63136.
- (29) Tăbăcaru, A.; Muşat, V.; Țigău, N.; Vasile, B. Ş.; Surdu, V.-A. Vinyltrimethoxysilane-Modified Zinc Oxide Quantum Dots with Tuned Optical Properties. *Appl. Surf. Sci.* **2015**, *359*, 766–773.
- (30) Buşilă, M.; Tăbăcaru, A.; Muşat, V.; Vasile, B. Ş.; Neaşu, I. A.; Pinheiro, T.; Roma-Rodrigues, C.; Baptista, P. V.; Fernandes, A. R.; Matos, A. P.; et al. Size-Dependent Biological Activities of Fluorescent Organosilane-Modified Zinc Oxide Nanoparticles. *J. Biomed. Nanotechnol.* **2020**, *16*, 137–152.
- (31) Wei, J.; Ji, G.; Zhang, C.; Yan, L.; Luo, Q.; Wang, C.; Chen, Q.; Yang, J.; Chen, L.; Ma, C.-Q. Silane-Capped ZnO Nanoparticles for Use as the Electron Transport Layer in Inverted Organic Solar Cells. *ACS Nano* **2018**, *12*, 5518–5529.
- (32) Singh, M.; Kaur, N.; Drera, G.; Casotto, A.; Ermenegildo, L. S.; Comini, E. SAM Functionalized ZnO Nanowires for Selective Acetone Detection: Optimized Surface Specific Interaction Using APTMS and GLYMO Monolayers. *Adv. Funct. Mater.* **2020**, 2003217.
- (33) Rohe, B.; Veeman, W. S.; Tausch, M. Synthesis and Photocatalytic Activity of Silane-Coated and UV-Modified Nanoscale Zinc Oxide. *Nanotechnology* **2006**, *17*, 277–282.
- (34) Kotecha, M.; Veeman, W.; Rohe, B.; Tausch, M. NMR Investigations of Silane-Coated Nano-Sized ZnO Particles. *Micropor. Mesopor. Mater.* **2006**, *95*, 66–75.
- (35) Bagnall, D. M.; Chen, Y. F.; Zhu, Z.; Yao, T.; Shen, M. Y.; Goto, T. High Temperature Excitonic Stimulated Emission from ZnO Epitaxial Layers. *Appl. Phys. Lett.* **1998**, *73*, 1038–1040.
- (36) Vanheusden, K.; Seager, C. H.; Warren, W. L.; Tallant, D. R.; Voigt, J. A. Correlation between Photoluminescence and Oxygen Vacancies in ZnO Phosphors. *Appl. Phys. Lett.* **1998**, *68*, 403–405.
- (37) Kohan, A. F.; Ceder, G.; Morgan, D.; Van de Walle, C. G. First-Principles Study of Native Point Defects in ZnO. *Phys. Rev. B* **2000**, *61*, 15019–15027.
- (38) Foley, M.; Ton-That, C.; Phillips, M. R. Cathodoluminescence Inhomogeneity in ZnO Nanorods. *Appl. Phys. Lett.* **2008**, *93*, 243104.
- (39) Bohle, D. S.; Spina, C. J. Cationic and Anionic Surface Binding Sites on Nanocrystalline Zinc Oxide: Surface Influence on Photoluminescence and Photocatalysis. *J. Am. Chem. Soc.* **2009**, *131*, 4397–4404.
- (40) McCluskey, M. D.; Jokela, S. J. Defects in ZnO. *J. Appl. Phys.* **2009**, *106*, 071101.
- (41) Ton-That, C.; Weston, L.; Phillips, M. R. Characteristics of Point Defects in the Green Luminescence from Zn- and O-Rich ZnO. *Phys. Rev. B* **2012**, *86*, 115205.
- (42) Gottschalk, H.; Patzer, G.; Alexander, H. Stacking Fault Energy and Ionicity of Cubic III–V Compounds. *Phys. Status Solidi A* **1978**, *45*, 207–217.
- (43) Fonoberov, V. A.; Alim, K. A.; Balandin, A. A.; Xiu, F.; Liu, J. Photoluminescence Investigation of the Carrier Recombination Processes in ZnO Quantum Dots and Nanocrystals. *Phys. Rev. B* **2006**, *73*.
- (44) Takeuchi, S.; Suzuki, K. Stacking Fault Energies of Tetrahedrally Coordinated Crystals. *Phys. Status Solidi C* **1999**, *171*, 99–103.
- (45) Langford, J. I.; Boulton, A.; Auffredic, J. P.; Louer, D. The Use of Pattern Decomposition to Study the Combined X-Ray Diffraction Effects of Crystallite Size and Stacking Faults in Ex-Oxalate Zinc Oxide. *J. Appl. Cryst.* **1993**, *26*, 22–33.
- (46) Niederdraenk, F.; Seufert, K.; Stahl, A.; Bhalerao-Panjkar, R. S.; Marathe, S.; Kulkarni, S. K.; Nader, R. B.; Kumpf, C. Ensemble Modeling of Very Small ZnO Nanoparticles. *Phys. Chem. Chem. Phys.* **2011**, *13*, 498–505.
- (47) Bøjesen, E. D.; Jensen, K. M. Ø.; Tyrsted, C.; Lock, N.; Christensen, M.; Iversen, B. B. In Situ Powder Diffraction Study of the Hydrothermal Synthesis of ZnO Nanoparticles. *Cryst. Growth Des.* **2014**, *14*, 2803–2810.
- (48) Khranovskyy, V.; Eriksson, M. O.; Radnoczi, G. Z.; Khalid, A.; Zhang, H.; Holtz, P. O.; Hultman, L.; Yakimova, R. Photoluminescence Study of Basal Plane Stacking Faults in ZnO Nanowires. *Physica B* **2014**, *439*, 50–53.
- (49) Yan, Y.; Dalpian, G. M.; Al-Jassim, M. M.; Wei, S.-H. Energetics and Electronic Structure of Stacking Faults in ZnO. *Phys. Rev. B* **2004**, *70*, 193206.
- (50) Bertolotti, F.; Moscheni, D.; Guagliardi, A.; Masciocchi, N. When Crystals Go Nano - The Role of Advanced X-Ray Total Scattering Methods in Nanotechnology. *Eur. J. Inorg. Chem.* **2018**, *2018*, 3789–3803.
- (51) Debye, P. Zerstreuung von Röntgenstrahlen. *Ann. Phys.* **1915**, *351*, 809–823.
- (52) Billinge, S. J. L.; Levin, I. The Problem with Determining Atomic Structure at the Nanoscale. *Science* **2007**, *316*, 561–565.
- (53) Cervellino, A.; Frison, R.; Masciocchi, N.; Guagliardi, A. X-Ray and Neutron Techniques for Nanomaterials Characterization; Kumar, C. S. S. R., Ed.; Springer-Verlag GmbH Germany: Berlin, Germany, 2016; pp 545–608.
- (54) Frison, R.; Cernuto, G.; Cervellino, A.; Zaharko, O.; Colonna, G. M.; Guagliardi, A.; Masciocchi, N. Magnetite–Maghemite Nanoparticles in the 5–15 nm Range: Correlating the Core–Shell Composition and the Surface Structure to the Magnetic Properties. A Total Scattering Study. *Chem. Mater.* **2013**, *25*, 4820–4827.
- (55) Delgado-López, J. M.; Frison, R.; Cervellino, A.; Gómez-Morales, J.; Guagliardi, A.; Masciocchi, N. Crystal Size, Morphology, and Growth Mechanism in Bio-Inspired Apatite Nanocrystals. *Adv. Funct. Mater.* **2014**, *24*, 1090–1099.
- (56) Bertolotti, F.; Dirin, D. N.; Ibanez, M.; Krumeich, F.; Cervellino, A.; Frison, R.; Voznyy, O.; Sargent, E. H.; Kovalenko, M. V.; Guagliardi, A.; et al. Crystal Symmetry Breaking and Vacancies in Colloidal Lead Chalcogenide Quantum Dots. *Nat. Mater.* **2016**, *15*, 987–994.
- (57) Bertolotti, F.; Moscheni, D.; Migliori, A.; Zacchini, S.; Cervellino, A.; Guagliardi, A.; Masciocchi, N. A Total Scattering Debye Function Analysis Study of Faulted Pt Nanocrystals Embedded in a Porous Matrix. *Acta Cryst. A* **2016**, *72*, 632–644.
- (58) Bertolotti, F.; Protesescu, L.; Kovalenko, M. V.; Yakunin, S.; Cervellino, A.; Billinge, S. J. L.; Terban, M. W.; Pedersen, J. S.; Masciocchi, N.; Guagliardi, A. Coherent Nanotwins and Dynamic Disorder in Cesium Lead Halide Perovskite Nanocrystals. *ACS Nano* **2017**, *11*, 3819–3831.
- (59) Moscheni, D.; Bertolotti, F.; Piveteau, L.; Protesescu, L.; Dirin, D. N.; Kovalenko, M. V.; Cervellino, A.; Pedersen, J. S.; Masciocchi, N.; Guagliardi, A. Size-Dependent Fault-Driven Relaxation and Faceting in Zn-blende CdSe Colloidal Quantum Dots. *ACS Nano* **2018**, *12*, 12558–12570.
- (60) Bertolotti, F.; Nedelcu, G.; Vivani, A.; Cervellino, A.; Masciocchi, N.; Guagliardi, A.; Kovalenko, M. V. Crystal Structure, Morphology, and Surface Termination of Cyan-Emissive, Six-Monolayers-Thick CsPbBr<sub>3</sub> Nanoplatelets from X-Ray Total Scattering. *ACS Nano* **2019**, *13*, 14294–14307.
- (61) Bertolotti, F.; Vivani, A.; Moscheni, D.; Ferri, F.; Cervellino, A.; Masciocchi, N.; Guagliardi, A. Structure, Morphology, and Faceting of TiO<sub>2</sub> Photocatalysts by the Debye Scattering Equation Method. The P25 and P90 Cases of Study. *Nanomaterials* **2020**, *10*, 743.
- (62) Bertolotti, F.; Carmona, F. J.; Dal Sasso, G.; Ramírez-Rodríguez, G. B.; Delgado-López, J. M.; Pedersen, J. S.; Ferri, F.; Masciocchi, N.; Guagliardi, A. On the Amorphous Layer in Bone Mineral and Biomimetic Apatite: A Combined Small- and Wide-Angle X-Ray Scattering Analysis. *Acta Biomater.* **2021**, *120*.
- (63) Willmott, P. R.; Meister, D.; Leake, S. J.; Lange, M.; Bergamaschi, A.; Bøge, M.; Calvi, M.; Cancellieri, C.; Casati, N.; Cervellino, A.; et al. The Materials Science Beamline Upgrade at the Swiss Light Source. *J. Synchrotron Rad.* **2013**, *20*, 667–682.
- (64) Bergamaschi, A.; Cervellino, A.; Dinapoli, R.; Gozzio, F.; Henrich, B.; Johnson, I.; Kraft, P.; Mozzanica, A.; Schmitt, B.; Shi, X.



The MYTHEN Detector for X-Ray Powder Diffraction Experiments at the Swiss Light Source. *J. Synchrotron Radiat.* **2010**, *17*, 653–668.

(65) Cervellino, A.; Frison, R.; Bertolotti, F.; Guagliardi, A. DEBUSSY 2.0: The New Release of a Debye User System for Nanocrystalline and/or Disordered Materials. *J. Appl. Cryst.* **2015**, *48*, 2026–2032.

(66) Cervellino, A.; Giannini, C.; Guagliardi, A. On the Efficient Evaluation of Fourier Patterns for Nanoparticles and Clusters. *J. Comput. Chem.* **2006**, *27*, 995–1008.

(67) Nelder, J. A.; Mead, R. A Simplex Method for Function Minimization. *Comput. J.* **1965**, *7*, 308–313.

(68) Pandey, D. A Geometrical Notation for Stacking Faults in Close-Packed Structures. *Acta Cryst. B* **1984**, *40*, 567–569.

(69) Aboulaich, A.; Tilmaciu, C.-M.; Merlin, C.; Mercier, C.; Guiloteau, H.; Medjahdi, G.; Schneider, R. Physicochemical Properties and Cellular Toxicity of (Poly)Aminoalkoxysilanes-Functionalized ZnO Quantum Dots. *Nanotechnology* **2012**, *23*, 335101.

(70) Tang, E.; Liu, H.; Sun, L.; Zheng, E.; Cheng, G. Fabrication of Zinc Oxide/Poly(Styrene) Grafted Nanocomposite Latex and Its Dispersion. *Eur. Polym. J.* **2007**, *43*, 4210–4218.

(71) Niznansky, D.; Rehspringer, J. L. Infrared Study of SiO<sub>2</sub> Sol to Gel Evolution and Gel Aging. *J. Non-Cryst. Solids* **1995**, *180*, 191–196.

(72) Wahab, S. A. A.; Matori, K. A.; Aziz, S. H. A.; Zaid, M. H. M.; Kechik, M. M. A.; Azman, A. Z. K.; Khaidir, R. E. M.; Khiri, M. Z. A.; Effendy, N. Effect of ZnO on the Phase Transformation and Optical Properties of Silicate Glass Frits Using Rice Husk Ash as a SiO<sub>2</sub> Source. *J. Mater. Res. Technol.* **2020**, *9*, 11013–11021.

(73) Sato, M.; Matsuda, S. Structure of Vaterite and Infrared Spectra. *Z. Kristallogr.* **1969**, *129*, 405–410.

(74) Wahab, R.; Ansari, S. G.; Kim, Y. S.; Dar, M. A.; Shin, H.-S. Synthesis and Characterization of Hydrozincite and Its Conversion into Zinc Oxide Nanoparticles. *J. Alloy Compd.* **2008**, *461*, 66–71.

(75) Coenen, K.; Gallucci, F.; Mezari, B.; Hensen, E.; van Sint Annaland, M. An In-Situ IR Study on the Adsorption of CO<sub>2</sub> and H<sub>2</sub>O on Hydrotalcites. *J. CO<sub>2</sub> Util.* **2018**, *24*, 228–239.

(76) Warren, B. E. *X-Ray Diffraction*; Dover Publications, Series Ed.; Dover Books on Physics; New York, 1990.

(77) Wilson, A. J. C. *X-Ray Optics - The Diffraction of X-Rays by Finite and Imperfect Crystals*; Methuen & Co Ltd: London, 1962.

(78) Leineweber, A. Understanding Anisotropic Microstrain Broadening in Rietveld Refinement. *Z. Kristallogr.* **2011**, *226*, 905–923.

(79) Ulbrich, K. F.; Bertolotti, F.; Masciocchi, N.; Cervellino, A.; Guagliardi, A.; Campos, C. E. M. A Comprehensive Structural and Microstructural Investigation of a New Iron–Telluride Nano Phase. *J. Mater. Chem. C* **2018**, *6*, 3047–3057.

(80) Scardi, P.; Ermrich, M.; Fitch, A.; Huang, E.-W.; Jardin, R.; Kuzel, R.; Leineweber, A.; Mendoza Cuevas, A.; Misture, S. T.; Rebuffi, L.; et al. Size–Strain Separation in Diffraction Line Profile Analysis. *J. Appl. Cryst* **2018**, *51*, 831–843.

(81) Cernuto, G.; Masciocchi, N.; Cervellino, A.; Colonna, G. M.; Guagliardi, A. Size and Shape Dependence of the Photocatalytic Activity of TiO<sub>2</sub> Nanocrystals: A Total Scattering Debye Function Study. *J. Am. Chem. Soc.* **2011**, *133*, 3114–3119.

(82) Qiu, X.; Thompson, J. W.; Billinge, S. J. L. PDFgetX2: A GUI-Driven Program to Obtain the Pair Distribution Function from X-Ray Powder Diffraction Data. *J. Appl. Cryst* **2004**, *37*, 678–678.

(83) Spanhel, L. Colloidal ZnO Nanostructures and Functional Coatings: A Survey. *J. Sol-Gel Sci Technol* **2006**, *39*, 7–24.

(84) Leszczyński, M. K.; Justyniak, I.; Zelga, K.; Lewiński, J. From Ethylzinc Guanidinate to [Zn<sub>10</sub>O<sub>4</sub>] Supertetrahedron. *Dalton Trans.* **2017**, *46*, 12404–12407.

(85) Jang, E. S.; Won, J. H.; Hwang, S. J.; Choy, J. H. Fine Tuning of the Face Orientation of ZnO Crystals to Optimize Their Photocatalytic Activity. *Adv. Mat.* **2006**, *18*, 3309–3312.

(86) Zeng, J. H.; Jin, B. B.; Wang, Y. F. Facet Enhanced Photocatalytic Effect with Uniform Single-Crystalline Zinc Oxide Nanodisks. *Chem. Phys. Lett.* **2009**, *472*, 90–95.

(87) Zhang, L.; Yin, L.; Wang, C.; Lun, N.; Qi, Y. Sol-Gel Growth of Hexagonal Faceted ZnO Prism Quantum Dots with Polar Surfaces for Enhanced Photocatalytic Activity. *ACS Appl. Mater. Interfaces* **2010**, *2*, 1769–1773.

(88) Boppella, R.; Anjaneyulu, K.; Basak, P.; Manorama, S. V. Facile Synthesis of Face Oriented ZnO Crystals: Tunable Polar Facets and Shape Induced Enhanced Photocatalytic Performance. *J. Phys. Chem. C* **2013**, *117*, 4597–4605.

(89) Na, S.-H.; Park, C.-H. First-Principles Study of the Surface of Wurtzite ZnO and ZnS - Implications for Nanostructure Formation. *J. Korean Phys. Soc.* **2009**, *54*, 867–872.

(90) Stampfl, C.; Van de Walle, C. G. Energetics and Electronic Structure of Stacking Faults in AlN, GaN, and InN. *Phys. Rev. B* **1998**, *57*, R15052–R15055.

(91) Ohno, Y.; Koizumi, H.; Taishi, T.; Yonenaga, I.; Fujii, K.; Goto, H.; Yao, T. Optical Properties of Dislocations in Wurtzite ZnO Single Crystals Introduced at Elevated Temperatures. *J. Appl. Phys.* **2008**, *104*, 073515.

(92) Moghaddam, E.; Youzbashi, A. A.; Kazemzadeh, A.; Eshraghi, M. J. Photoluminescence Investigation of ZnO Quantum Dots Surface Modified with Silane Coupling Agent as a Capping Agent. *J. Lumin.* **2015**, *168*, 158–162.

(93) Peng, Y.-K.; Ye, L.; Qu, J.; Zhang, L.; Fu, Y.; Teixeira, I. F.; McPherson, I. J.; He, H.; Tsang, S. C. E. Trimethylphosphine-Assisted Surface Fingerprinting of Metal Oxide Nanoparticle by <sup>31</sup>P Solid-State NMR: A Zinc Oxide Case Study. *J. Am. Chem. Soc.* **2016**, *138*, 2225–2234.

## SYNOPSIS TOC.

A comprehensive quantitative model of vinyltrimethoxysilane-grafted ultrasmall ZnO nanocrystals is developed to elucidate the complex interplay of size, morphology, lattice strain, stacking faults and surface modification on electronic, optical and photocatalytic properties. Band gap narrowing upon downsizing is explained by planar defects with linear density as large as  $1.6 \times 10^6 \text{ cm}^{-1}$ .

